



Diagnosing systematic effects using the inferred initial power spectrum

Tristan Hoellinger ^{a)} and Florent Leclercq ^{b)}

Sorbonne Université, CNRS, UMR 7095, Institut d'Astrophysique de Paris, 98 bis bd Arago, 75014 Paris, France

(Dated: 18 July 2025)

The next generation of galaxy surveys has the potential to substantially deepen our understanding of the Universe. This potential hinges on our ability to rigorously address systematic uncertainties. Until now, diagnosing systematic effects prior to inferring cosmological parameters has been out of reach in field-based implicit likelihood cosmological inference frameworks. As a solution, we aim to diagnose a variety of systematic effects in galaxy surveys prior to inferring cosmological parameters, using the inferred initial matter power spectrum. Our approach is built upon a two-step framework. First, we employed the Simulator Expansion for Likelihood-Free Inference (SELI) algorithm to infer the initial matter power spectrum, which we utilised to thoroughly investigate the impact of systematic effects. This investigation relies on a single set of N -body simulations. Second, we obtained a posterior on cosmological parameters via implicit likelihood inference, recycling the simulations from the first step for data compression. As a demonstration, we relied on a model of large-scale spectroscopic galaxy surveys that incorporates fully non-linear gravitational evolution with COmoving Lagrangian Acceleration (COLA) and simulates multiple systematic effects encountered in real surveys. We provide a practical guide on how the SELI posterior can be used to assess the impact of misspecified galaxy bias parameters, selection functions, survey masks, inaccurate redshifts, and approximate gravity models on the inferred initial matter power spectrum. We show that a subtly misspecified model can lead to a bias exceeding 2σ in the (Ω_m, σ_8) plane, which we are able to detect and avoid prior to inferring cosmological parameters. This framework has the potential to significantly enhance the robustness of physical information extraction from full forward models of large-scale galaxy surveys such as DESI, *Euclid*, and LSST.

I. INTRODUCTION

Current and forthcoming large-scale galaxy surveys have the statistical capability to unveil the nature of dark energy, shed light on the mechanisms driving cosmic inflation, and constrain neutrino masses with unprecedented precision (Mishra-Sharma, Alonso & Dunkley, 2018; *Euclid* Collaboration, 2020; Goldstein *et al.*, 2023). The vast volumes of data collected by Stage-IV surveys (Albrecht *et al.*, 2006) such as DESI (DESI Collaboration, 2016), *Euclid* (*Euclid* Collaboration, 2024), and LSST (LSST Dark Energy Science Collaboration, 2012; Ivezić *et al.*, 2019) will be dominated by systematic rather than statistical uncertainties (Salvati, Douspis & Aghanim, 2020). Extracting the subtle signals relating to the cosmological structure and content of our Universe therefore requires careful treatment of astrophysical and observational nuisances, along with their associated systematic effects (e.g. Meiksin, White & Peacock, 1999; Desjacques, Jeong & Schmidt, 2018). Such effects are pervasive and constitute one of the foremost challenges in modern cosmology (e.g. Kim *et al.*, 2004; Kitching, Taylor & Heavens, 2008; Davis *et al.*, 2011; Kitching *et al.*, 2016; Glanville, Howlett & Davis, 2021; Ayçoberry *et al.*, 2023). For instance, substantial effort is being directed towards accurately measuring the growth rate of structure from peculiar velocities and galaxy surveys, whilst properly accounting for biases and selection effects (e.g. Said *et al.*, 2020; Carreres *et al.*, 2023). Crucially,

the risk of mistaking systematic biases for new physics must be rigorously addressed.

To match the ever-growing precision of observations from stage-IV astrophysical surveys, Bayesian cosmological inference pipelines rely on increasingly complex probabilistic simulators. In particular, field-based forward models of galaxy surveys have become a cornerstone of modern precision cosmology (e.g. Jasche & Wandelt, 2013; Leclercq, Jasche & Wandelt, 2015; Ramanah *et al.*, 2019; Porqueres *et al.*, 2022; Andrews *et al.*, 2023; Kostić *et al.*, 2023; Nguyen *et al.*, 2024; Zeghal *et al.*, 2024; Zhou *et al.*, 2024). These models simulate the evolution of the entire density field from its initial conditions in the early Universe to the present epoch. Whilst these simulators incorporate a refined treatment of non-linear gravitational evolution, astrophysical nuisances, and instrumental responses, the resulting pipelines become increasingly dependent on the accuracy of the underlying models. Consequently, they exhibit little to no robustness to model misspecification: when models deviate from the actual data-generating process, posteriors tend to become biased or overly concentrated (Frazier, Robert & Rousseau, 2017). For instance, using explicit likelihood inference within an effective field theory model of large-scale structure, Nguyen *et al.* (2021) showed that misspecified models can significantly bias the inferred transfer function.

Current approaches to cosmological data analysis using field-based models can be classified into two broad categories, depending on whether the likelihood is explicitly or implicitly defined. Explicit likelihood methods (e.g. Wandelt, Larson & Lakshminarayanan, 2004; Jasche & Wandelt, 2013; Wang *et al.*, 2014, 2016; Als-

^{a)}tristan.hoellinger@iap.fr; <https://hoellin.github.io/>

^{b)}florent.leclercq@iap.fr; <https://www.florent-leclercq.eu/>

ing *et al.*, 2016; Jasche & Lavaux, 2019; Loureiro *et al.*, 2023; Sellentin *et al.*, 2023; Zhou *et al.*, 2024) employ Markov chain Monte Carlo (MCMC, Metropolis *et al.*, 1953) algorithms such as Hamiltonian Monte Carlo (HMC, Duane *et al.*, 1987) to sample from the target distribution. To make the likelihood tractable, they rely on approximations of the astronomical observables’ models. In contrast, implicit likelihood approaches (see Weyant, Schafer & Wood-Vasey, 2013; Ishida *et al.*, 2015; Lintusaari *et al.*, 2017; Alsing, Wandelt & Feeney, 2018; Leclercq, 2018; Leclercq *et al.*, 2019; Taylor *et al.*, 2019; Alsing *et al.*, 2019; Brehmer *et al.*, 2018; Cranmer, Brehmer & Louppe, 2020; Makinen *et al.*, 2021; Nguyen *et al.*, 2024; Tucci & Schmidt, 2024; Ho *et al.*, 2024, for reviews and applications to cosmology) can accommodate arbitrarily complex simulator-based models, in which the internal mechanisms are unknown or difficult to incorporate into likelihood-based analyses. We refer to these simulators as hidden-box models. They may include a physical treatment of structure formation through N -body simulations as well as the intricacies of observational processes within the survey.

Both explicit and implicit approaches are susceptible to model misspecification. To address this issue within explicit likelihood cosmological inference frameworks, several solutions have been proposed: developing flexible data models (Jasche & Lavaux, 2017, 2019; Nguyen *et al.*, 2021; Porqueres *et al.*, 2022), marginalising over unknown systematic effects (Porqueres *et al.*, 2019), heating up the likelihood (Jasche & Lavaux, 2019), or informing the likelihood with explicit knowledge of where the model is likely to underperform (Doeser *et al.*, 2024). Some statistical literature has recently been focused on addressing the issue of model misspecification in Implicit Likelihood Inference (ILI, e.g. Thomas *et al.*, 2020). Yet, until now, no method had been designed to systematically address model misspecification in field-based implicit likelihood cosmological inferences.

Among the ILI approaches to cosmological data analysis, Leclercq *et al.* (2019) introduced the Simulator Expansion for Likelihood-Free Inference (SELFIE) algorithm, which makes it possible to infer the initial matter power spectrum using arbitrarily complex hidden-box models of galaxy surveys. The initial matter power spectrum (after recombination) is a theoretically well-understood object, and we expect its inference to be sensitive to most of the systematic effects encountered in the survey. Therefore, in this paper, we propose to use the initial matter power spectrum to diagnose systematic effects in implicit likelihood cosmological inferences from hidden-box models of galaxy surveys.

The full pipeline that we construct is built upon an application to cosmological data analysis of the two-step procedure introduced by Leclercq (2022) for ILI of Bayesian Hierarchical Models (BHMs) where a latent function carries relevant information about the target parameters to be inferred. The latent function is further required to be confined within a narrow region

of its parameter space. Cosmological inferences naturally fall within this class of BHMs: the initial matter power spectrum can be treated as a latent function within the physical model mapping the cosmological parameters to the observed galaxy count fields; and its shape is already strongly constrained by Cosmic Microwave Background experiments (Planck Collaboration, 2020; Balkenhol *et al.*, 2023). For the first step of the procedure, we utilise the SELFIE algorithm to infer the initial matter power spectrum. The inference requires the mean data model at an expansion point along with its gradient, which can be estimated by finite differences as in Leclercq *et al.* (2019). Alternatively, manual or automatic differentiation can be used: see Hahn, List & Porqueres (2024) for an automatically differentiable Boltzmann solver; Wang *et al.* (2014); Jasche & Lavaux (2019); Modi, Lanusse & Seljak (2021) for differentiable N -body simulators; PINETREE (Ding, Lavaux & Jasche, 2024) for a differentiable halo model. The second step of the procedure addresses the primary objective of inferring the cosmological parameters given the observations. Any ILI technique such as Approximate Bayesian Computation (ABC) or more sophisticated techniques can be used.¹ ILI is known to be arduous when the dimensionality of the data space is high (e.g. Cranmer, Brehmer & Louppe, 2020), and therefore requires data compression. A benefit of the statistical framework introduced by Leclercq (2022) is that the simulations generated in the first step naturally provide a score compressor (Heavens, Jimenez & Lahav, 2000; Alsing & Wandelt, 2018) for the second step at no additional cost.

In this article, we illustrate the method with a forward model of spectroscopic galaxy surveys that includes fully non-linear gravitational evolution and simulates multiple systematic effects. We use a prior embedding substantial information about the initial matter power spectrum, building upon previous experiments to effectively reduce the dimensionality of the parameter space, and infer the initial matter power spectrum from synthetic observations using SELFIE. To make things simple whilst keeping an ILI framework, we rely on an ABC procedure using a Population Monte Carlo (ABC-PMC) sampler (Beaumont *et al.*, 2009) to infer the posterior on cosmological parameters. Using the ABC posterior, we show that an inconspicuously misspecified model can lead to a bias greater than 2σ in the (Ω_m, σ_8) plane. This bias can be unambiguously detected and avoided before performing the ILI of cosmological parameters. We provide a practical guide to diagnose systematic effects in implicit likelihood cosmological inferences, demonstrating how the SELFIE posterior enables a comprehensive investigation of misspecified linear galaxy bias parameters, selection functions, survey masks, and inaccurate redshifts. Importantly, this process relies on a single, tractable set

¹ If the likelihood of the model has an explicit form, explicit likelihood techniques may also be used for the second step.

of N -body simulations. Additionally, at the cost of using distinct sets of N -body simulations, we are able to investigate the effect of misspecified gravity models, which is not directly apparent from the error on the galaxy count fields.

This article is structured as follows. In Section II, we introduce the BHM used in this work and describe the two-step framework in detail, with a novel treatment of cosmological parameters within the hidden-box model compared to the original version of the SELFIE algorithm. In Section III, we present the spectroscopic galaxy survey model used in this study, which includes a non-linear physical model of structure formation and accounts for multiple observational systematic effects. In Section IV, we address the issue of model misspecification by investigating the impact of systematic effects on the inferred initial matter power spectrum, and we discuss their impact on the posterior on cosmological parameters. Finally, we discuss our results and conclude in Section V.

II. METHOD

A. Bayesian hierarchical models of galaxy surveys with the initial matter power spectrum as a latent vector

We consider a BHM comprising the following variables: the target parameters $\boldsymbol{\omega} \in \mathbb{R}^N$, limited to cosmological parameters in this paper, a latent vector $\boldsymbol{\theta} \in \mathbb{R}^S$, corresponding to the normalised values of the initial matter power spectrum at S wave numbers, the summary statistics $\boldsymbol{\Phi} \in \mathbb{R}^P$ of the mock galaxy populations considered in this study, and the compressed data vector $\tilde{\boldsymbol{\omega}} \in \mathbb{R}^N$ composed of N numbers—one per target parameter. The deterministic compression step $\tilde{\mathcal{C}}$ linking $\boldsymbol{\Phi}$ to $\tilde{\boldsymbol{\omega}}$ is discussed in Section II C 1. A graphical representation of the generic BHM is presented in Figure 1; additionally, Figure 2 provides a detailed representation of the BHM in the context of cosmological inference from probing the large-scale structure of the Universe. In applications aimed at jointly constraining cosmological and astrophysical nuisance parameters from upcoming galaxy surveys, we expect $N \sim \mathcal{O}(5 - 20)$ target parameters, $S \sim \mathcal{O}(10^2 - 10^3)$; P can be as large as $\mathcal{O}(10^4)$ for complex data models exploiting information beyond 2-point statistics, and corresponds to a first layer of compression from the D -dimensional full-field data, which may be as large as $D \sim \mathcal{O}(10^{11})$. Table I provides an overview of the different variables appearing in this section and their respective physical interpretation within the spectroscopic galaxy survey model introduced for this study.

In this work, the variables $\boldsymbol{\omega}$ and $\boldsymbol{\theta}$ are linked by a deterministic Boltzmann solver, the Cosmic Linear Anisotropy Solving System (CLASS, Blas, Lesgourgues & Tram, 2011), which associated with the deterministic function \mathcal{T} in the BHM. Alternative choices include the Code for Anisotropies in the Microwave Background (CAMB, Lewis & Challinor, 2011), Differentiable Simu-

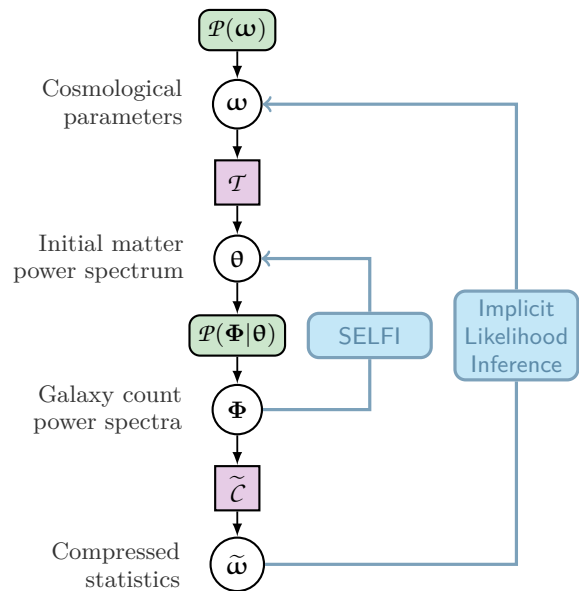


FIG. 1. Hierarchical representation of the Bayesian framework employed for diagnosing model misspecification and inferring the target parameters $\boldsymbol{\omega}$. The rounded green boxes denote probability distributions, whilst the purple squares represent deterministic functions. $\mathcal{P}(\boldsymbol{\omega})$ is the prior on $\boldsymbol{\omega}$. \mathcal{T} is a deterministic function linking $\boldsymbol{\omega}$ to $\boldsymbol{\theta}$. $\mathcal{P}(\boldsymbol{\Phi}|\boldsymbol{\theta})$ denotes the probabilistic data model that maps the space of latent vectors $\boldsymbol{\theta}$ to the survey space. The final layer, $\tilde{\mathcal{C}}$, is a deterministic compression step required for the ILI of the target parameters $\boldsymbol{\omega}$. In this study, $\boldsymbol{\omega}$ is the vector of cosmological parameters, \mathcal{T} is derived from the Boltzmann solver CLASS, $\boldsymbol{\theta}$ is the initial matter power spectrum (after recombination), and $\boldsymbol{\Phi}$ corresponds to the power spectra of multiple galaxy number count fields.

lations for COsmology — Done with Jax (DISCO-DJ, Hahn, List & Porqueres, 2024), an emulator of cosmological power spectra (Spurio Mancini *et al.*, 2022; Mootoovaloo *et al.*, 2022) or a fitting function such as the Eisenstein-Hu fitting function (Eisenstein & Hu, 1998; Campagne *et al.*, 2023). In either case, \mathcal{T} is theoretically well-understood and numerically inexpensive compared to the potentially misspecified part of the BHM, which is the probabilistic simulator $\mathcal{P}(\boldsymbol{\Phi}|\boldsymbol{\theta})$ linking the initial matter power spectrum $\boldsymbol{\theta}$ to the simulated summary statistic $\boldsymbol{\Phi}$.

A.1 The top-level Bayesian problem

From a broad perspective, the cosmological inference problem considered here consists in updating prior knowledge $\mathcal{P}(\boldsymbol{\omega})$ of the cosmological parameters $\boldsymbol{\omega}$ through the Bayes rule

$$\mathcal{P}(\boldsymbol{\omega}|\boldsymbol{\Phi}_O) = L_{\boldsymbol{\omega}}(\boldsymbol{\omega}) \frac{\mathcal{P}(\boldsymbol{\omega})}{\mathcal{P}(\boldsymbol{\Phi}_O)}, \quad (1)$$

TABLE I. Main variables, their generic role in the statistical framework, and their physical interpretation in this study.

Symbol	Role in the BHM	Physical meaning in this work
$\boldsymbol{\omega} \in \mathbb{R}^N$	Target parameters	Cosmological parameters h , Ω_m , Ω_b , n_S and σ_8 , corresponding to $N = 5$.
$\boldsymbol{\theta} \in \mathbb{R}^S$	Latent vector	Vectorial parametrisation of the initial matter power spectrum over $S = 64$ support points.
$\boldsymbol{\psi} \in \mathbb{R}^T$	Nuisance parameters	Random numbers involved in the phase and noise realisations.
$\mathbf{o} \in \mathbb{R}^N$	Target parameters treated as nuisance parameters	Cosmological parameters h , Ω_m , Ω_b , n_S and σ_8 at play inside the probabilistic simulator $\mathcal{P}(\boldsymbol{\Phi} \boldsymbol{\theta})$, which is the second part of the BHM, used for the latent vector inference. The symbol \mathbf{o} is introduced to avoid confusion with $\boldsymbol{\omega}$ in the first part of the BHM.
$\mathbf{d} \in \mathbb{R}^D$	Full data vector	Three-dimensional maps of the galaxy number counts in the survey volume for the three mock populations of galaxies. $D = 3 \cdot 512^3 \simeq 4 \times 10^8$.
$\boldsymbol{\Phi} \in \mathbb{R}^P$	Summary statistics	Power spectra of the galaxy number count fields. We use the concatenation of the three 27-dimensional estimated power spectra for each galaxy population, so $P = 111$.
$\boldsymbol{\Phi}_O \in \mathbb{R}^P$	Observed summary statistics	Power spectra of the observed galaxy number count fields. The capital letter ‘‘O’’ stands for ‘‘Observations’’.
$\tilde{\boldsymbol{\omega}} \in \mathbb{R}^N$	Compressed summaries	Summary statistics of the galaxy number count fields after data compression.

TABLE II. The variables’ roles within the BHM are defined in Section II A. We elaborate upon their physical interpretations in Section III, which describes the large-scale spectroscopic galaxy survey model used in this study.

based on observations $\boldsymbol{\Phi}_O$ from one or multiple cosmological probes, where the true, unknown likelihood with respect to the cosmological parameters is given by

$$L_{\boldsymbol{\omega}}(\boldsymbol{\omega}) \equiv \mathcal{P}(\boldsymbol{\Phi}_O|\boldsymbol{\omega}), \quad (2)$$

and the prior $\mathcal{P}(\boldsymbol{\omega})$ stems from previous experiments and/or encodes physical constraints derived from theoretical considerations and heuristic rules. From this point onwards, to avoid assuming a parametric form for the likelihood $L_{\boldsymbol{\omega}}(\boldsymbol{\omega})$, we employ ILI techniques based on a probabilistic forward model of the observable $\boldsymbol{\Phi}$. These techniques rely on comparing the simulated data, $\boldsymbol{\Phi}$, with the observations $\boldsymbol{\Phi}_O$, which is difficult when the dimension P of the summarised data space is high. Consequently, the observed and simulated data must undergo an additional compression step, denoted by $\tilde{\mathcal{C}}$ in Figure 1.

A.2 The latent vector inference

To obtain a posterior for the initial matter power spectrum $\boldsymbol{\theta}$ conditional on the observations $\boldsymbol{\Phi}_O$, we consider the alternative inference problem defined by

$$\mathcal{P}(\boldsymbol{\theta}|\boldsymbol{\Phi}_O) \propto L(\boldsymbol{\theta})\mathcal{P}(\boldsymbol{\theta}), \quad (3)$$

where

$$L(\boldsymbol{\theta}) \equiv \mathcal{P}(\boldsymbol{\Phi}_O|\boldsymbol{\theta}) \quad (4)$$

is the true intermediate likelihood. We expect the inference of $\boldsymbol{\theta}$ to be sensitive to most of the systematic effects of interest, as the initial matter power spectrum contains a wealth of information about the cosmological parameters $\boldsymbol{\omega}$ (Peebles, 1980). Harnessing our theoretical understanding of $\boldsymbol{\theta}$, we use the posterior $\mathcal{P}(\boldsymbol{\theta}|\boldsymbol{\Phi}_O)$

as a diagnostic tool to examine how simulation- and observation-related systematic effects may affect the top-level Bayesian inference problem defined by Equation (2).

B. First step: Initial matter power spectrum inference

B.1 The power spectrum prior distribution

At wave number k , we define the latent vector as

$$\theta_k \equiv \frac{P(k)}{P_0(k)}, \quad (5)$$

where $P(k)$ is the initial matter power spectrum, and the normalisation function $P_0(k)$ is the Bardeen-Bond-Kaiser-Szalay (BBKS, Bardeen *et al.*, 1986) power spectrum for some fiducial cosmological parameters $\boldsymbol{\omega}_0$. The normalisation P_0 plays no role in the statistical framework presented here and is introduced solely for numerical stability, as initial power spectra span several orders of magnitude across the range of scales considered.

We assume that, given a prior $\mathcal{P}(\boldsymbol{\omega})$, a tight, physically-motivated prior on the initial matter power spectrum $\boldsymbol{\theta}$ can be obtained by sampling from $\mathcal{P}(\boldsymbol{\omega})$ and propagating the samples through the Boltzmann solver associated with the deterministic function \mathcal{T} . That is, $\mathcal{P}(\boldsymbol{\theta}|\boldsymbol{\omega}) = \delta_{\boldsymbol{\theta}}^D(\mathcal{T}(\boldsymbol{\omega}))$, where $\delta_{\boldsymbol{\theta}}^D$ is the Dirac measure centred on $\boldsymbol{\theta}$. Marginalising over $\boldsymbol{\omega}$ yields:

$$\mathcal{P}(\boldsymbol{\theta}) = \int \delta_{\boldsymbol{\theta}}^D(\mathcal{T}(\boldsymbol{\omega}))\mathcal{P}(\boldsymbol{\omega}) d\boldsymbol{\omega}. \quad (6)$$

To obtain an explicit form for $\mathcal{P}(\boldsymbol{\theta})$, we assume a Gaussian-distributed prior on the initial matter power spectrum, whose mean and covariance matrix can be estimated by drawing from Equation (6). We generate an

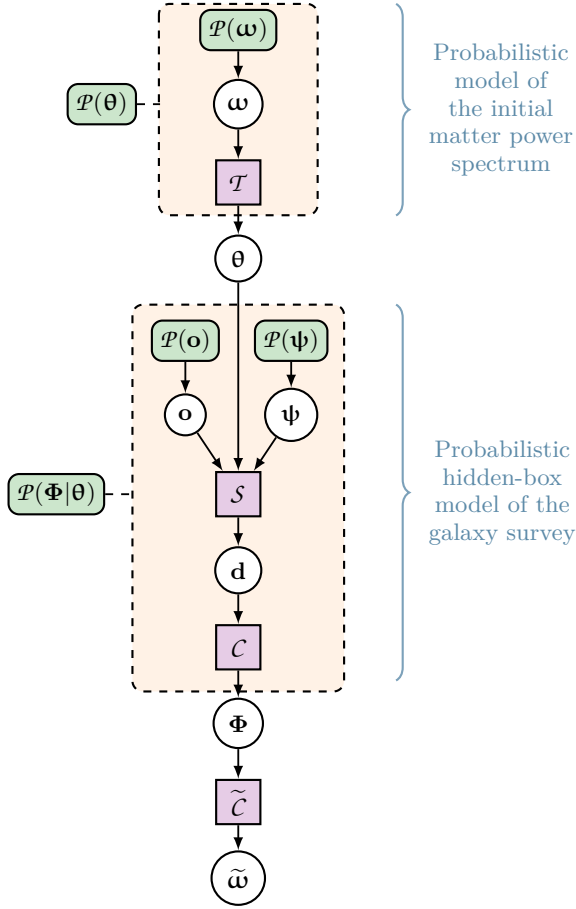


FIG. 2. Detailed representation of the BHM used in this study for the inference of cosmological parameters ω from galaxy surveys. The hidden-box model corresponds to the second dashed orange rectangle and defines the true (unknown) likelihood $L(\theta)$ when $\Phi = \Phi_0$. The variables are ω (the target cosmological parameters), θ (the initial matter power spectrum), ψ (the nuisance parameters), \mathbf{o} (the cosmological parameters, formally treated as nuisance parameters within the hidden-box), \mathbf{d} (the full data vector containing the full galaxy count fields), Φ (the summary statistics), and $\tilde{\omega}$ (the compressed summaries). We provide further details about the roles and physical meanings of these variables in Table I.

ensemble of m simulated power spectra $\theta_{\omega}^{(i)} = \mathcal{T}(\omega^{(i)})$, $i \in \llbracket 1, m \rrbracket$, where $\omega^{(i)} \sim \mathcal{P}(\omega)$. The resulting prior reads

$$-2 \log \mathcal{P}(\theta) \equiv \log |2\pi \mathbf{S}| + \left\| \theta - \hat{\theta}_{\omega} \right\|_{\mathbf{S}^{-1}}^2, \quad (7)$$

where we introduced the notation $\|\mathbf{a}\|_{\mathbf{B}}^2 \equiv \mathbf{a}^{\top} \mathbf{B} \mathbf{a}$, with

$$\hat{\theta}_{\omega} \equiv \mathbb{E}^m [\theta_{\omega}] = \frac{1}{m} \sum_{i=1}^m \theta_{\omega}^{(i)} \quad (8)$$

the mean of our prior, and where

$$\begin{aligned} \mathbf{S} &\equiv \frac{m}{m-1} \mathbb{E}^m \left[(\theta_{\omega} - \hat{\theta}_{\omega})(\theta_{\omega} - \hat{\theta}_{\omega})^{\top} \right] \\ &= \frac{1}{m-1} \sum_{i=1}^m (\theta_{\omega}^{(i)} - \hat{\theta}_{\omega})(\theta_{\omega}^{(i)} - \hat{\theta}_{\omega})^{\top} \end{aligned} \quad (9)$$

is the empirical prior covariance matrix. The symbol \mathbb{E}^m denotes the empirical mean computed from an ensemble of m samples.

Since evaluating the deterministic function \mathcal{T} is computationally inexpensive compared to the probabilistic simulator $\mathcal{P}(\Phi|\theta)$, m can be taken as large as necessary to ensure that the prior distribution $\mathcal{P}(\theta)$ is well-sampled. In this work, we use $m = 10^4$.

B.2 The power spectrum posterior distribution

In the following, we adopt the approach introduced by [Leclercq et al. \(2019\)](#) to obtain a posterior on θ , with the key distinction that we formally treat the cosmological parameters \mathbf{o} as additional nuisance parameters within the hidden-box model, over which we marginalise. In doing so, we rigorously account for the dependence of the mapping from initial matter power spectra to evolved dark matter density fields on the cosmological parameters.

Once realisations of θ , \mathbf{o} , and ψ are specified, the output $\mathbf{d} \in \mathbb{R}^D$ of the simulation is a deterministic function \mathcal{S} ; that is, $\mathcal{P}(\mathbf{d}|\theta, \mathbf{o}, \psi) = \delta_{\mathbf{d}}^D(\mathcal{S}(\theta, \mathbf{o}, \psi))$, where, again, $\delta_{\mathbf{d}}^D$ denotes the Dirac measure centred on \mathbf{d} . Including the compression \mathcal{C} of the full data \mathbf{d} to a summary statistic Φ , the hidden-box model can therefore be expressed as $\mathcal{B} \equiv \mathcal{C} \circ \mathcal{S}$, as illustrated in Figure 2. Marginalising over \mathbf{o} and ψ , the exact likelihood given by Equation (4) reads

$$\begin{aligned} L(\theta) &= \int \mathcal{P}(\Phi_0|\theta, \mathbf{o}, \psi) \mathcal{P}(\mathbf{o}) \mathcal{P}(\psi) \, \mathrm{d}\mathbf{o} \, \mathrm{d}\psi \\ &= \int \delta_{\Phi_0}^D(\mathcal{B}(\theta, \mathbf{o}, \psi)) \mathcal{P}(\mathbf{o}) \mathcal{P}(\psi) \, \mathrm{d}\mathbf{o} \, \mathrm{d}\psi, \end{aligned} \quad (10)$$

which involves an intractable integral.

To overcome this difficulty, an inefficient yet insightful approach is to condition the probabilities on an ensemble of θ -dependent data realisations. For a given θ , consider an ensemble of K simulated summaries $\Phi_{\theta}^{(i)} = \mathcal{B}(\theta, \mathbf{o}^{(i)}, \psi^{(i)})$ with $i \in \llbracket 1, K \rrbracket$, where K is arbitrary for now. Postulating an effective Gaussian likelihood yields $\tilde{L}^K(\theta) = \exp[\tilde{\ell}^K(\theta)]$ with the effective log-likelihood $\tilde{\ell}^K(\theta)$ defined as

$$-2\tilde{\ell}^K(\theta) = \log |2\pi \hat{\Sigma}_{\theta}'| + \left\| \Phi_0 - \hat{\Phi}_{\theta} \right\|_{\hat{\Sigma}_{\theta}'^{-1}}^2, \quad (11)$$

where $\hat{\Phi}_{\theta}$ is the empirical mean of the simulated sum-

maries, defined by

$$\hat{\Phi}_{\theta} \equiv \mathbb{E}^K [\Phi_{\theta}] = \frac{1}{K} \sum_{i=1}^K \Phi_{\theta}^{(i)}, \quad (12)$$

and the estimators of the covariance matrix of $\tilde{L}^K(\theta)$ and its inverse are given by:

$$\begin{aligned} \frac{K-1}{K+1} \hat{\Sigma}'_{\theta} &\equiv \mathbb{E}^K [(\Phi_{\theta} - \hat{\Phi}_{\theta})(\Phi_{\theta} - \hat{\Phi}_{\theta})^{\top}] \\ &= \frac{1}{K} \sum_{i=1}^K (\Phi_{\theta}^{(i)} - \hat{\Phi}_{\theta})(\Phi_{\theta}^{(i)} - \hat{\Phi}_{\theta})^{\top} \text{ and} \\ \frac{K+1}{K} \hat{\Sigma}'_{\theta}{}^{-1} &\equiv \alpha \hat{\Sigma}_{\theta}^{-1}, \end{aligned} \quad (13)$$

respectively. The factor $\alpha \equiv \frac{K-P-2}{K-1}$ arises from the assumption that Σ_{θ}^{-1} follows an inverse-Wishart distribution (Hartlap, Simon & Schneider, 2007); the $\frac{K+1}{K}$ factor originates from a derivation of $\tilde{L}^K(\theta)$ based on a surrogate signal proposed in Leclercq *et al.* (2019), which motivates the Gaussian parametric form.

At this point, the numerical cost of computing $\tilde{L}^K(\theta)$ as given by Equation (11) is still prohibitively large when the full parameter space has to be explored: it requires K simulations per θ where an evaluation of the approximate likelihood is sought. The SELFI algorithm solves this issue by Taylor-expanding the full forward model at first order around an expansion point θ_0 , leveraging prior knowledge of the initial matter power spectrum so that the linearised model remains asymptotically exact around θ_0 . We define the expansion point as

$$\theta_0 \equiv \mathcal{T}(\omega_0), \quad (14)$$

where ω_0 is a vector of fiducial cosmological parameters.

The aforementioned approach translates into a linearisation of the mean data model around the initial matter power spectrum θ_0 . Namely, let \mathbf{o} and $\boldsymbol{\psi}$ denote cosmological and nuisance parameters, $\delta\theta$ be a small vector in the parameter space; let $\mathbf{X}_0 = (\theta_0, \mathbf{o}, \boldsymbol{\psi})$, $\mathbf{H} = (\delta\theta, 0, 0)$, $\mathbf{X} = \mathbf{X}_0 + \mathbf{H}$. At first order in its first variable, $\mathcal{B}(\mathbf{X}) \equiv \mathcal{C} \circ \mathcal{S}(\mathbf{X})$ can be approximated by

$$\begin{aligned} \mathcal{B}_j(\mathbf{X}) &\simeq \mathcal{B}_j(\mathbf{X}_0) + \nabla \mathcal{B}_j(\mathbf{X}_0) \cdot \mathbf{H} \\ &\simeq \mathcal{B}_j(\mathbf{X}_0) + \partial_{\theta} \mathcal{B}_j(\mathbf{X}_0) \cdot \delta\theta, \end{aligned} \quad (15)$$

where $\mathcal{B}_j(\mathbf{X})$ is the j -th component of $\mathcal{B}(\mathbf{X})$ and ∂_{θ} denotes the partial derivative with respect to the initial matter power spectrum. Formally treating the cosmological parameters \mathbf{o} intervening in the second layer of the BHM as a nuisance and marginalising over all nuisances yields

$$\begin{aligned} \mathbb{E}[\Phi_{\theta}] &\equiv \int \mathcal{B}(\mathbf{X}) \mathcal{P}(\mathbf{o}) \mathcal{P}(\boldsymbol{\psi}) \, \mathrm{d}\mathbf{o} \, \mathrm{d}\boldsymbol{\psi} \\ &\simeq \int [\mathcal{B}(\mathbf{X}_0) + \partial_{\theta} \mathcal{B}(\mathbf{X}_0) \delta\theta] \mathcal{P}(\mathbf{o}) \mathcal{P}(\boldsymbol{\psi}) \, \mathrm{d}\mathbf{o} \, \mathrm{d}\boldsymbol{\psi} \\ &\simeq \mathbb{E}[\mathcal{B}(\mathbf{X}_0)] + \partial_{\theta} \mathbb{E}[\mathcal{B}(\mathbf{X}_0)] \cdot \delta\theta, \end{aligned} \quad (16)$$

under the assumption that the \mathbb{E} and ∂_{θ} operators can be permuted in Equation (16), and where the expectation is taken with respect to the joint distribution of \mathbf{o} and $\boldsymbol{\psi}$. For any θ , the ensemble mean $\mathbb{E}[\Phi_{\theta}]$ can therefore be approximated by

$$\mathbf{f}(\theta) \equiv \mathbf{f}_0 + \nabla_{\theta} \mathbf{f}_0 \cdot \delta\theta, \quad (17)$$

where $\delta\theta = \theta - \theta_0$, $\mathbf{f}_0 \equiv \mathbb{E}^{N_0}[\Phi_{\theta_0}]$ is the empirical mean of the data model at the expansion point θ_0 using N_0 simulations for different phase and other nuisance realisations, and $\nabla_{\theta} \mathbf{f}_0$ is the empirical gradient of \mathcal{B} .

Further assuming the covariance matrix to be independent of θ close to the expansion point, that is $\hat{\Sigma}'_{\theta} \simeq \hat{\Sigma}'_{\theta_0} \equiv \mathbf{C}_0$, and replacing the exact data model in Equation (11) with the linearised data model \mathbf{f} , the SELFI effective likelihood is given by $\hat{L}^{N_0}(\theta) = \exp[\hat{\ell}_{\theta}^{N_0}(\theta)]$ with

$$-2\hat{\ell}_{\theta}^{N_0}(\theta) \equiv \log |2\pi \mathbf{C}_0| + \|\Phi_{\theta} - \mathbf{f}(\theta)\|_{\mathbf{C}_0^{-1}}^2. \quad (18)$$

At the end of the day, SELFI approximates the average hidden-box model with its linearisation \mathbf{f} around θ_0 marginalised over the nuisance parameters. These assumptions, alongside the Gaussian effective likelihood assumption, solely impact the inference of the initial matter power spectrum θ , and do not affect the inference of the target cosmological parameters $\boldsymbol{\omega}$ discussed later, except through data compression.

The SELFI likelihood defined by Equation (18) is fully characterised by \mathbf{f}_0 , \mathbf{C}_0 , and $\nabla_{\theta} \mathbf{f}_0$, which can all be evaluated through forward simulations. The numerical computation requires N_0 simulations at the expansion point to evaluate \mathbf{f}_0 and \mathbf{C}_0 . The gradient $\nabla_{\theta} \mathbf{f}_0$ can be evaluated using an analytical formula or auto-differentiation when available. In this work, we perform N_s simulations in each direction of the parameter space to empirically estimate $\nabla_{\theta} \mathbf{f}_0$ via first-order forward finite differences. The total number of simulations required is therefore $N_{\text{tot}} = N_0 + N_s \times S$ simulations. N_0 and N_s should be of the order of the dimensionality of the data space P , giving a total cost of $\mathcal{O}(\gtrsim P(S+1))$ model evaluations. If not chosen in advance, a precise value for N_0 and N_s can be obtained by ensuring sufficient convergence of the covariance matrix and the gradients (see Appendix A) or by monitoring the convergence of the SELFI posterior.

To fully characterise the Bayesian problem, any prior $\mathcal{P}(\theta)$ can be used, such as the prior naturally given by Equation (6). Any numerical technique such as MCMC can then be employed to explore the posterior using Equation (18), which does not require any additional evaluation of the hidden-box model. Remarkably, if the prior is Gaussian, then the SELFI effective posterior for the initial matter power spectrum is Gaussian and reads:

$$-2 \log \mathcal{P}(\theta | \Phi_{\theta}) \simeq \log |2\pi \Gamma| + \|\theta - \boldsymbol{\gamma}\|_{\Gamma^{-1}}, \quad (19)$$

with mean and covariance matrix given by

$$\boldsymbol{\gamma} \equiv \theta_0 + \Gamma (\nabla_{\theta} \mathbf{f}_0)^{\top} \mathbf{C}_0^{-1} (\Phi_{\theta} - \mathbf{f}_0) + \Gamma \mathbf{S}^{-1} \Delta, \quad (20)$$

$$\Gamma \equiv [(\nabla_{\theta} \mathbf{f}_0)^{\top} \mathbf{C}_0^{-1} \nabla_{\theta} \mathbf{f}_0 + \mathbf{S}^{-1}]^{-1}. \quad (21)$$

$\Delta = \hat{\theta}_\omega - \theta_0$ is the difference between the prior mean and the expansion point. This result was derived by [Leclercq *et al.* \(2019\)](#) for the special case where the mean of the prior is equal to the expansion point; that is, $\Delta = 0$. We provide the general derivation in Appendix B. To avoid inverting \mathbf{S} in case it is ill-conditioned, one may equivalently opt for the alternative form:

$$\Gamma \mathbf{S}^{-1} \Delta = [\mathbf{S}(\nabla_\theta \mathbf{f}_0)^\top \mathbf{C}_0^{-1} \nabla_\theta \mathbf{f}_0 + \mathbf{I}]^{-1} \Delta, \quad (22)$$

$$\Gamma = [\mathbf{S}(\nabla_\theta \mathbf{f}_0)^\top \mathbf{C}_0^{-1} \nabla_\theta \mathbf{f}_0 + \mathbf{I}]^{-1} \mathbf{S}. \quad (23)$$

B.3 Check for model misspecification

A sensitivity analysis of how systematic effects in the data model influence the posterior θ can be performed by recalculating the SELFI posterior mean γ using Equation (20) whilst varying the model of the systematic effect under investigation. This approach enables qualitative assessments of the impact of model misspecification on the posterior initial matter power spectrum, which can be interpreted in light of theoretical considerations. For a given posterior, as a simple quantitative check for model misspecification, we compute the Mahalanobis distance between the reconstruction γ and the prior distribution $\mathcal{P}(\theta)$:

$$d_M(\gamma, \theta_0 | \mathbf{S}) \equiv \|\gamma - \theta_0\|_{\mathbf{S}^{-1}}. \quad (24)$$

We compare it to an ensemble of values of $d_M(\theta, \theta_0 | \mathbf{S})$ for simulations $\theta = \mathcal{T}(\omega)$, where ω is drawn from $\mathcal{P}(\omega)$.

C. Second step: Implicit likelihood inference of the cosmological parameters

C.1 Score compression

The second step of the framework focuses on inferring the cosmological parameters ω based on the observations Φ_O . As usual in ILI, the simulated and observed summaries must undergo an additional compression step to reduce their dimensionality. In essence, the compressed summaries $\tilde{\mathcal{C}}(\Phi)$ should closely approximate sufficient statistics of Φ , such that $\mathcal{P}(\omega | \tilde{\mathcal{C}}(\Phi)) \simeq \mathcal{P}(\omega | \Phi)$. Following the procedure described by [Leclercq \(2022\)](#), we assume, for compression only, that $\mathcal{P}(\Phi | \omega)$ is Gaussian-distributed: $\mathcal{P}(\Phi | \omega) \equiv \exp[\hat{\ell}_\omega(\omega)]$ with $\hat{\ell}_\omega(\omega) \equiv \hat{\ell}(\mathcal{T}(\omega))$, where

$$-2\hat{\ell}_\omega(\omega) \equiv \log |2\pi \mathbf{C}_0| + \|\Phi_O - \mathbf{f}[\mathcal{T}(\omega)]\|_{\mathbf{C}_0^{-1}}^2 \quad (25)$$

is the effective log-likelihood defined in the first part of the framework by Equation (18), which corresponds to the exact log-likelihood under the Gaussian assumption.

We consider the score function $\nabla_\omega \hat{\ell}_\omega$, which is the gradient of the log-likelihood with respect to the parameters ω at a fiducial point in parameter space. This function is a sufficient statistic for the log-likelihood given by Equation (25) to linear order ([Alsing & Wandelt, 2018](#)), making it a natural choice for data compression. Using ω_0 as the fiducial point, a quasi maximum-likelihood estimator for the parameters is given by $\tilde{\omega}_O = \omega_0 + \mathbf{F}_0^{-1} \nabla_\omega \hat{\ell}_\omega(\omega_0)$ where the Fisher matrix $\mathbf{F}_0 = \mathbb{E}[\nabla \hat{\ell}_\omega(\omega_0) \nabla^\top \hat{\ell}_\omega(\omega_0)]$ represents the expected observed information, and the gradient of the log-likelihood is evaluated at ω_0 . Compression of Φ_O to $\tilde{\omega}_O$ yields N compressed statistics, which are optimal in the sense that they saturate the Fisher information content of the data at the expansion point under lenient assumptions provided by [Alsing & Wandelt \(2018\)](#).

Further assuming that the covariance \mathbf{C}_0 does not depend on the parameters ($\nabla_\omega \mathbf{C}_0 = 0$) around the expansion point, and using Equation (14), the compressor can be approximated by

$$\tilde{\mathcal{C}}(\Phi) \equiv \tilde{\omega} \equiv \omega_0 + \mathbf{F}_0^{-1} [(\nabla_\omega \mathbf{f}_0)^\top \mathbf{C}_0^{-1} (\Phi - \mathbf{f}_0)], \quad (26)$$

where the Fisher matrix is given by

$$\mathbf{F}_0 \equiv -\mathbb{E}[\nabla_\omega \nabla_\omega \hat{\ell}_\omega(\omega_0)] = (\nabla_\omega \mathbf{f}_0)^\top \mathbf{C}_0^{-1} \nabla_\omega \mathbf{f}_0, \quad (27)$$

with $\nabla_\omega \mathbf{f}_0 = \nabla \mathbf{f}_0 \cdot \nabla_\omega \mathcal{T}(\omega_0)$ ([Heavens, Jimenez & Lahav, 2000](#); [Alsing & Wandelt, 2018](#)). [Alsing & Wandelt \(2018\)](#) provide a more general data compression scheme which includes the case when the dependence of \mathbf{C}_0 on the parameter cannot be neglected.

At this point, \mathbf{C}_0 and $\nabla \mathbf{f}_0$ have already been computed for the initial matter power spectrum inference with SELFI; and the gradient $\nabla_\omega \mathcal{T}(\omega_0)$ derived from the Boltzmann solver can easily be computed for instance by finite difference or using auto-differentiation ([Hahn, List & Porqueres, 2024](#)). We now have a BHM that maps the N target parameters, ω , to the same number N of compressed summaries, $\tilde{\omega}$, as summarised in Figure 1, which can be used to infer the target cosmological parameters using standard ILI techniques.

C.2 Implicit likelihood inference with a population Monte Carlo sampler

Every ILI method, such as ABC, requires a discrepancy measure to compare the compressed simulated summaries $\tilde{\omega}$ with the observed summaries $\tilde{\omega}_O$ ([Beaumont, Zhang & Balding, 2002](#); [Sunnåker *et al.*, 2013](#)). For this purpose, we re-used the Fisher matrix from Equation (27) to compute the Fisher-Rao distance between the compressed observed and simulated data, defined by:

$$d_{\text{FR}}(\tilde{\omega}, \tilde{\omega}_O) \equiv \|\tilde{\omega} - \tilde{\omega}_O\|_{\mathbf{F}_0}. \quad (28)$$

To infer the target parameters $\tilde{\omega}$ given the observed summaries, $\tilde{\omega}_O$, we relied on a simple yet theoretically

well-motivated particle filter method, which is a variant introduced by [Simola *et al.* \(2021\)](#) of ABC-PMC. Unlike the basic ABC sampling strategy, known as implicit likelihood rejection sampling ([Neumann, 1951](#); [Beaumont, Zhang & Balding, 2002](#)), and which does not take advantage of the information acquired during the sampling process, particle filters iteratively refine pools of candidates—referred to as particles, bringing them closer and closer to the true posterior distribution. Specifically, ABC-PMC methods gradually enhance the quality of the samples by updating the proposal distribution.

The ABC-PMC algorithm variant introduced by [Simola *et al.* \(2021\)](#) and employed here proceeds as follows. First, we set an initial acceptance threshold ϵ_0 , and generated an initial pool of J particles $\Xi^{(0)} \equiv \left\{ \boldsymbol{\omega}_i^{(0)} \right\}_{i \in [1, J]}$ by drawing cosmological parameters from the proposal distribution $\pi^{(0)}(\boldsymbol{\omega}) \equiv \mathcal{P}(\boldsymbol{\omega})$ until they satisfied $d_{\text{FR}}(\tilde{\mathcal{C}} \circ \mathcal{B}(\boldsymbol{\omega}_i^{(0)}), \tilde{\boldsymbol{\omega}}_O) < \epsilon_0$. This initial step is equivalent to an implicit likelihood rejection sampling stage with J accepted samples and a tolerance ϵ_0 .

To construct an intermediate proposal distribution $\pi^{(1)}(\boldsymbol{\omega})$ and the corresponding approximate posterior, the method uses a Gaussian mixture distribution. We set initial weights $w_i^{(0)} \equiv J^{-1}$. The initial multivariate Gaussian kernel functions are centred on $\boldsymbol{\omega}_i^{(0)}$, with a common covariance matrix defined as twice the weighted sample covariance of the particles $\Xi^{(0)}$; that is,

$$\boldsymbol{\Sigma}^{(0)} = 2 \sum_{i=1}^J w_i^{(0)} \left(\boldsymbol{\omega}_i^{(0)} - \hat{\boldsymbol{\omega}}^{(0)} \right) \left(\boldsymbol{\omega}_i^{(0)} - \hat{\boldsymbol{\omega}}^{(0)} \right)^\top, \quad (29)$$

where $\hat{\boldsymbol{\omega}}^{(0)}$ is the sample mean of the particles $\Xi^{(0)}$. The factor 2 arises from minimising the Kullback-Leibler divergence ([Kullback & Leibler, 1951](#)) between the proposal and the target distribution ([Beaumont *et al.*, 2009](#)). This leads to the updated proposal distribution

$$\pi^{(1)}(\boldsymbol{\omega}) = \sum_{i=1}^J w_i^{(0)} \mathcal{G} \left(\boldsymbol{\omega} \mid \boldsymbol{\omega}_i^{(0)}, \boldsymbol{\Sigma}^{(0)} \right), \quad (30)$$

where $\mathcal{G}(\boldsymbol{\omega} \mid \boldsymbol{\mu}, \boldsymbol{\Sigma})$ denotes the probability distribution function (pdf) of a Gaussian centred on $\boldsymbol{\mu}$ with covariance matrix $\boldsymbol{\Sigma}$, evaluated at $\boldsymbol{\omega}$.

In subsequent iterations t , the algorithm proceeds by drawing particles from the approximate posterior proposal distribution $\pi^{(t)}(\boldsymbol{\omega})$ until they satisfy $d_{\text{FR}}(\tilde{\mathcal{C}} \circ \mathcal{B}(\boldsymbol{\omega}_i^{(t)}), \tilde{\boldsymbol{\omega}}_O) < \epsilon_t$ for some $\epsilon_t < \epsilon_{t-1}$. This results in the updated pool of particles $\Xi^{(t)} = \left\{ \boldsymbol{\omega}_i^{(t)} \right\}_{i \in [1, J]}$, along with an updated proposal $\pi^{(t+1)}(\boldsymbol{\omega})$ given by the Gaussian mixture distribution

$$\pi^{(t+1)}(\boldsymbol{\omega}) = \sum_{i=1}^J w_i^{(t)} \mathcal{G} \left(\boldsymbol{\omega} \mid \boldsymbol{\omega}_i^{(t)}, \boldsymbol{\Sigma}^{(t)} \right), \quad (31)$$

where the unnormalised importance weights are

$$\tilde{w}_i^{(t)} \equiv \frac{\pi^{(t)}(\boldsymbol{\omega}_i^{(t)})}{\sum_{j=1}^J w_j^{(t-1)} \mathcal{G} \left(\boldsymbol{\omega}_i^{(t)} \mid \boldsymbol{\omega}_j^{(t-1)}, \boldsymbol{\Sigma}^{(t-1)} \right)}, \quad (32)$$

so that $w_i^{(t)} = \tilde{w}_i^{(t)} / \sum_j \tilde{w}_j^{(t)}$. The covariance matrix $\boldsymbol{\Sigma}^{(t)}$ is, again, defined as twice the weighted sample covariance of the particles $\Xi^{(t)}$. The resulting approximate posterior can thus be expressed as a kernel density estimator:

$$\hat{\pi}_{\epsilon_t, h}(\boldsymbol{\omega} \mid \tilde{\boldsymbol{\omega}}_O) = \sum_{i=1}^J w_i^{(t)} k_h \left(\boldsymbol{\omega} - \boldsymbol{\omega}_i^{(t)} \right), \quad (33)$$

where k_h is the kernel (e.g. [Rosenblatt, 1956](#); [Parzen, 1962](#)), and where we replaced the exponent (t) with ϵ_t to emphasise the dependence on the acceptance threshold. In this study, we used an isotropic Gaussian kernel with a smoothing parameter h . The particles were drawn from sequentially improving proposal distributions, with decreasing tolerances $\epsilon_0 > \epsilon_1 > \dots > \epsilon_T$. The algorithm starts with an initial acceptance quantile q_0 , which is fixed by the initial tolerance ϵ_0 , and terminates when q_T falls below a predetermined target quantile q . The target q sets the maximum allowable pointwise difference between posteriors at successive stages for the algorithm to be deemed converged. The rule for determining T and the choice of the decreasing sequence of tolerances are discussed in detail in [Simola *et al.* \(2021\)](#). The sequence is designed to ensure efficient sampling and to provide good exploration of the relevant regions of the parameter space. Starting from the initial acceptance quantile q_0 , subsequent tolerances were determined as follows:

$$\epsilon_t = \min_{i \in [1, J]} \left\{ d_{\text{FR}} \left(\tilde{\mathcal{C}} \circ \mathcal{B} \left(\boldsymbol{\omega}_i^{(t-1)} \right), \tilde{\boldsymbol{\omega}}_O \right) \right\}, \quad (34)$$

$$q_t = \left(\sup_{\boldsymbol{\omega}} \frac{\tilde{\pi}_{\epsilon_t}(\boldsymbol{\omega} \mid \tilde{\boldsymbol{\omega}}_O)}{\tilde{\pi}_{\epsilon_{t-1}}(\boldsymbol{\omega} \mid \tilde{\boldsymbol{\omega}}_O)} \right)^{-1}, \quad (35)$$

where $\tilde{\pi}_{\epsilon_t} / \tilde{\pi}_{\epsilon_{t-1}}$ is a density ratio estimate of the posterior change between steps $t-1$ and t . Notably, substantial differences between the approximate posteriors at stages $t-1$ and t lead to a large shrinkage of the proposed tolerance ϵ_{t+1} . The shrinkage in tolerance gradually decreases as the ABC posterior converges.

III. DATA MODEL OF GALAXY SURVEYS

In the following, Model A refers to the correct, well-specified model used to generate the synthetic observations, whilst Model B refers to a misspecified model.

A. Initial power spectrum parametrisation

Throughout this work, we defined the initial density fluctuations and galaxy overdensity fields on a cubic

equidistant grid with a comoving side length of $3.6 \text{ Gpc}/h$ and 512^3 voxels, spanning scales between $k_{s,\text{min}} = 1.75 \times 10^{-3} \text{ h/Mpc}$ and $k_{s,\text{max}} = 7.74 \times 10^{-1} \text{ h/Mpc}$. We discretised the parameter space by evaluating the continuous normalised power spectra at $S = 64$ support wave numbers k_s , yielding the vector $\boldsymbol{\theta}$ defined by Equation (5). Between two consecutive support wave numbers, we interpolated power spectra $P(k)$ using quintic splines. The first eight support wave numbers match the largest modes in the Fourier grid of our set-up. We manually distributed the remaining support wave numbers up to $k_{s,\text{max}}$ to ensure a small maximum relative error in the representation of initial matter power spectra across all wave numbers of the Fourier grid. We verified that, for all k below the grid’s Nyquist frequency, this set-up yielded a relative interpolation error below 0.14% for the fiducial power spectrum.

B. Gravitational evolution

The data model is a non-linear process meant to approximate the large variety of physical and observational phenomena at play in actual galaxy surveys. To generate dark matter overdensity fields for a given set of cosmological parameters, we essentially followed the procedure described by [Leclercq *et al.* \(2019\)](#). We assumed a flat Λ CDM cosmology ([Blumenthal *et al.*, 1984](#)) and used the best fit of the Planck 2018 ([Planck Collaboration, 2020](#)) data, given in Table III, as the fiducial cosmological parameters $\boldsymbol{\omega}_0$.

TABLE III. Fiducial cosmological parameters $\boldsymbol{\omega}_0$.

h	$\Omega_b h^2$	Ω_m	n_s	σ_8
0.6766	0.02242	0.3111	0.9665	0.8102

TABLE IV. Values taken from [Planck Collaboration \(2020\)](#).

Given an initial matter power spectrum $P(k)$, we generated a corresponding realisation of the initial matter density contrast field δ^i . For the gravitational evolution, we used the SIMBELMYNĚ cosmological solver ([Leclercq, Jasche & Wandelt, 2015](#)). We populated the initial grid of 512^3 voxels with 1024^3 dark matter particles arranged on a regular lattice. These particles were evolved via second order Lagrangian Perturbation Theory (2LPT) ([Moutarde *et al.*, 1991](#); [Bouchet *et al.*, 1995](#)) up to redshift $z_{\text{LPT}} = 19$, followed by N -body evolution with COLA (COmoving Lagrangian Acceleration, [Tassev, Zaldarriaga & Eisenstein, 2013](#)) from z_{LPT} to $z_1 = 0.1500$, both implemented within SIMBELMYNĚ. We performed the COLA evolution on a particle-mesh grid of 1024^3 voxels. We used 20 non-uniform time steps, which we distributed to ensure approximately linear scaling in the scale factor a while meeting the requirements imposed by our choice of mock galaxy populations. Specifically, the first 14 time steps were linearly spaced

in a up to redshift $z_3 = 0.8182$, followed by four time steps linearly spaced in a up to redshift $z_2 = 0.4925$, and finally two additional time steps to reach $z_1 = 0.1500$, corresponding to a scale factor of $a = 0.8696$.

The observer is positioned at one corner of the box, whereby they see one octant of the sky. Using the radial component v_r of their final peculiar velocities with respect to the observer, the dark matter particles are placed in redshift space according to the non-linear mapping defined for each particle by

$$1 + z_{\text{obs}} = (1 + z_{\text{cosmo}})(1 + z_{\text{pec}}), \quad z_{\text{pec}} \equiv -\frac{v_r}{c}, \quad (36)$$

where z_{cosmo} is the true cosmological redshift, z_{pec} is the redshift due to the peculiar velocity, z_{obs} is the “observed” redshift of the particle and c is the speed of light. The particles are then assigned to a 512^3 -voxels grid using the cloud-in-cell scheme ([Hockney & Eastwood, 1988](#)) to give the density contrast fields at redshift z_i , denoted δ^{z_i} , illustrated in the upper and middle rows of Figure 3.

C. Galaxy biasing

Galaxies are biased tracers of the underlying dark matter distribution ([Kaiser, 1984](#); [Bardeen *et al.*, 1986](#)). The mapping from local dark matter overdensities to the galaxy density field is a crucial element in cosmological inferences, involving numerous physical processes. Multiple questions, such as halo formation and mergers, gas cooling, and stellar feedback ([Desjacques, Jeong & Schmidt, 2018](#)), have to be addressed. Despite its inherent complexity, the highly non-linear process of galaxy formation can be accurately described by a small number of bias parameters on linear and quasi-linear scales, through a bias expansion in the matter density contrast and tidal fields. The parameters of this expansion often exhibit degeneracies with cosmological parameters, making the bias model critical in cosmological inferences, with the potential to either significantly enhance or severely bias the constraints on cosmological parameters ([Barreira, 2020](#); [Barreira *et al.*, 2020](#)). Consequently, exploiting galaxy survey data beyond Baryon Acoustic Oscillations (BAOs) requires careful modelling of galaxy biases ([Barreira, Lazeyras & Schmidt, 2021](#); [Beyond2pt Collaboration, 2024](#)), and there remains considerable scope for improving the bias models employed in cosmological analyses ([Bartlett, Ho & Wandelt, 2024](#)).

In this study, we focus on linear galaxy bias parameters, usually denoted b_1 in the literature, and use our framework to assess the impact of these bias parameters on the SELFI posterior on the initial matter power spectrum. The same statistical framework can be applied to study the impact of higher-order Local-In-Matter Density (LIMD) bias parameters or tidal bias parameters on the initial matter power spectrum reconstruction. We leave this exploration for future research. Hereafter, the first-order LIMD bias parameter for the i -th galaxy pop-

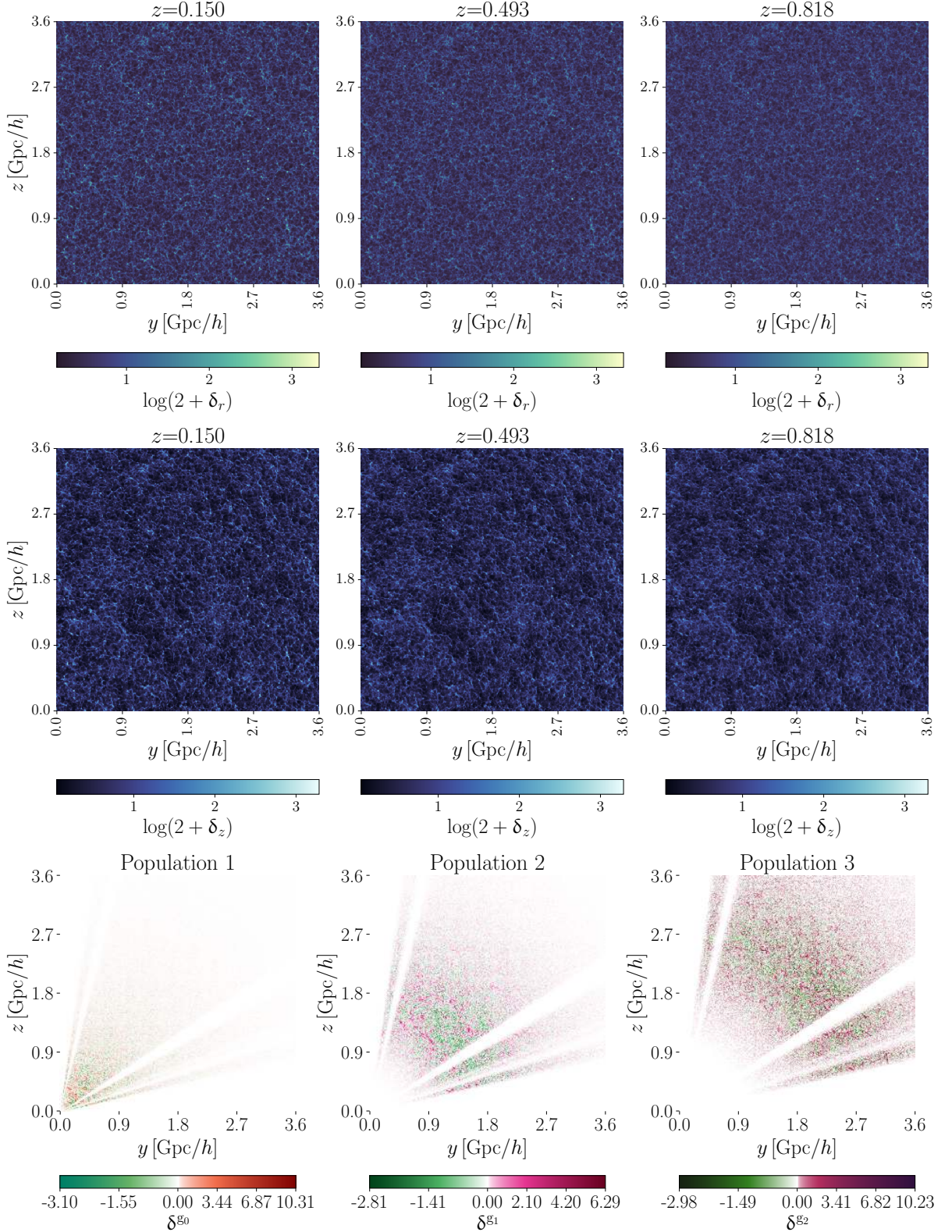


FIG. 3. Illustration of the galaxy survey data model used in this study. (Upper and middle rows) Slices through a realisation of the dark matter overdensity fields in real space (*top*) and redshift space (*middle*). The fields are evolved in time using N -body simulations, starting from a grid of Gaussian initial dark matter density fluctuations with power spectrum Θ_{gt} , up to the redshift indicated above the corresponding panels. (Lower row) Observed galaxy number count fields for the three galaxy populations, each defined on a grid of 512^3 cells. Light-cone effects are accounted for by using one effective redshift per galaxy population. Each slice passes through the observer located at the $(0, 0, 0)$ corner of the box.

ulation g_i is denoted b_{g_i} , to avoid confusion of b_{g_2} and b_{g_3} with higher order bias parameters.

We simulated three mock galaxy populations: one population of nearby bright galaxies and two populations of Luminous Red Galaxies (LRGs). LRGs are slowly evolving galaxies that have been extensively studied; due to their high spatial densities and intrinsic brightness, they are among the most valuable tracers of the dark matter distribution (Eisenstein *et al.*, 2001) in the Universe. Notably, subsamples of the 1.5 million spectra from the Baryon Oscillation Spectroscopic Survey (Eisenstein, 2015) have been prominently used to study the large-scale structure of the Universe, proving able to measure the BAOs in their large-scale distribution (Eisenstein *et al.*, 2005; Anderson *et al.*, 2014). LRGs are notably the primary target of DESI within the redshift range $0.4 < z < 1.0$ (Zhou *et al.*, 2023).

We approximated light cone effects by using snapshots from the dark matter overdensity field at three distinct redshifts z_1 , z_2 , and z_3 , as input to the linear bias model to define the three populations of galaxies, where z_i represents the effective redshift of the i -th galaxy population g_i . According to the linear bias model, the normalised galaxy density ρ^{g_i} for the galaxy population g_i is therefore given in any cell x by:

$$\rho_x^{g_i} = \bar{N} (1 + b_{g_i} \delta_x^{z_i}). \quad (37)$$

For simplicity, we used fixed values for the b_{g_i} parameters, given in Table V. We emphasise that, given any prior distribution for these parameters, they could be treated as additional nuisances alongside ψ and marginalised over, without affecting the statistical framework presented in this article. To showcase the efficiency of our method for diagnosing systematic effects with high signal-to-noise ratio data, we made the simplifying assumption that $\bar{N} = 1$, effectively adopting a unit system where the mean number of galaxies per cell equals unity, which in turn affects the stochastic properties of the galaxy count fields, as detailed in Section III D. We further assumed that the contrast,

$$\delta_x^{g_i} = b_{g_i} \delta_x^{z_i}, \quad (38)$$

could be observed directly, implying in particular that the mean number of galaxies per cell is perfectly known.

TABLE V. Linear galaxy bias parameters used in this study.

Model	Population 1	Population 2	Population 3
A	1.47	1.99	2.32
B	1.50	1.98	2.33

To simulate LRG populations, we based our approach on the measurements reported by Gil-Marín *et al.* (2015), where the authors found $b_1^{1.40}(z_{\text{eff}})\sigma_8(z_{\text{eff}}) = 1.672 \pm 0.060$ and $f\sigma_8(z_{\text{eff}}) = 0.597$ for $z_{\text{eff}} = 0.57$ (best fit of their full sample), yielding $b_1^{1.40}(z_{\text{eff}}) = 2.80 \pm 0.10$. Motivated by the (b_1, D) degeneracy between the linear galaxy bias and

the growth factor at large scales, we assumed constant $b_1(z)D(z)$ within the relevant redshift range, yielding:

$$b_1(z) \simeq \frac{b_1(z_{\text{eff}}) \times D(z_{\text{eff}})}{D(z)} \simeq \frac{2.086 \times D(z_{\text{eff}})}{D(z)}. \quad (39)$$

For the two LRGs populations, g_2 and g_3 , we applied Equation (39) to the mean redshift of each bin, used as the effective redshift to estimate an approximate ground truth linear bias (see Figure 4 and table V). For nearby galaxies, we used the measurements $f\sigma_8(z_1 = 0.15) = 0.43_{-0.14}^{+0.15}$ and $b_1\sigma_8(z_1 = 0.15) = 1.20 \pm 0.15$ provided for a sample of high-bias galaxies at $z < 0.2$ by Howlett *et al.* (2015). Assuming $f = \Omega_m^{0.55}$ (Bouchet *et al.*, 1995), we obtained $b_1(z_1 = 0.15) \simeq 1.45$. For Model A, we randomly selected the ground truth values in a ± 0.02 interval around those given by the above equations. For Model B, the misspecified values were chosen manually. They are reported in Table V.

D. Observational processes

The last step involves a virtual observation of the galaxy fields, accounting for observational effects expected in actual surveys. One such effect is dust extinction. Dust particles in the Milky Way and the intergalactic medium, presumably ejected by stars, absorb a significant portion of UV-to-near-infrared light, contaminating observations, causing reddening that must be corrected for (Galametz *et al.*, 2017), and affecting the noise properties of the observed galaxies (Ho *et al.*, 2015). The presence of gas and plasma in the intra- and extra-galactic medium introduces another known source of attenuation, as these media absorb, scatter, and re-emit a portion of incident radiation at longer wavelengths (Ménard *et al.*, 2008; More, Bovy & Hogg, 2009).

These attenuation phenomena, along with contamination from bright stars, constitute complex and often correlated systematic effects (Boulanger *et al.*, 1996) which can significantly impact nearly all cosmological measurements, from supernova distance estimates (Brout & Riess, 2023) to photometric and spectroscopic galaxy surveys (Corasanti, 2006; Leistedt & Peiris, 2014; Ho *et al.*, 2015; Bovy *et al.*, 2016). Consequently, considerable effort is devoted to accurately modelling and accounting for dust extinction in cosmological inference pipelines (e.g. Huterer, Cunha & Fang, 2013; Jasche & Lavaux, 2017; Karchev *et al.*, 2024).

To obtain the simulated data from the galaxy contrast fields, we computed the three-dimensional survey response operators \mathbf{W}_i . For each galaxy population g_i , the corresponding operator is defined as the product of the radial selection function, $R_i(r)$, and the angular survey mask and completeness function $C(\hat{\mathbf{n}})$ for any line of sight $\hat{\mathbf{n}}$; that is,

$$\mathbf{W}_i(\hat{\mathbf{n}}, r) \equiv R_i(r) C(\hat{\mathbf{n}}). \quad (40)$$

For the angular completeness $C(\hat{\mathbf{n}})$, we used a mask mimicking the wide sky coverage of stage-IV experiments, shown in Figure 5. We introduced additional linear extinction near the galactic plane up to 60° galactic latitude as a simple model of dust extinction. We also introduced 256 randomly positioned holes of angular diameter $\sim 0.1^\circ$, representing the masking of bright stars or other point sources contamination expected in galaxy surveys. Then, we projected the octant delineated by the light orchid triangle in Figure 5 onto the observed 512^3 grid to define the survey mask. We modelled the radial selection functions as log-normal distributions in redshift, which approximately captures the expected behaviour over a range of redshifts (as in e.g. [Gavazzi & Jaffe, 1986](#)). They are defined by

$$R_i(z) = \frac{c_i}{z\sigma_i\sqrt{2\pi}} \left[\exp\left(-\frac{(\ln z - \mu_i)^2}{2\sigma_i^2}\right) \right], \quad (41)$$

where the constants σ_i and μ_i take different values for the three galaxy populations, and c_i scales the amplitude of the signal. By analogy with the scaling of redshift uncertainties in typical photometric survey models (e.g. [Laureijs *et al.*, 2011](#)), we defined the variance s_i of the log-normal selection functions in our data model as

$$s_i = s(1 + z_i), \quad (42)$$

with an overall factor $s = 0.1$, where z_i is the effective redshift of the i -th galaxy population. The R_i are defined in redshift using $\mu_i \equiv \ln\left(z_i^2/\sqrt{z_i^2 + s_i^2}\right)$ and $\sigma_i^2 = \ln\left(1 + s_i^2/z_i^2\right)$, and then mapped to distance space using tabulated values of the distance-redshift relation. The values of z_i , s_i , and c_i used for Models A and B are provided in Table VI; the corresponding profiles of the selection functions are illustrated in Figure 4.

TABLE VI. Values of the selection function parameters.

Parameter	g_1	g_2	g_3
z_i	0.1500	0.4925	0.8182
s_i	0.1150	0.1493	0.1818
c_i (Model A)	0.1638	0.1638	0.1638
c_i (Model B)	0.1638	0.1605	0.1670

TABLE VII. The values are reported to the fourth decimal place. Only the c_i values differ between Models A and B.

We emulated the survey by generating galaxy excess number counts $N_x^{g_i}$ for each cell x of the box across the three galaxy populations. To account for instrumental noise, the $N_x^{g_i}$ were drawn from Gaussian distributions with means $\mu_x^{g_i}$ and standard deviations $\varsigma_{i,x}$,

$$N_x^{g_i} \sim \mathcal{G}(\mu_x^{g_i}, \varsigma_{i,x}). \quad (43)$$

The mean $\mu_x^{g_i} \equiv W_{i,x} b_{g_i} \delta_x^{z_i}$ characterises the expected number of galaxies based on Equation (38), where $W_{i,x}$ is the value in the cell x of the three-dimensional response operator defined by Equation (40). The standard

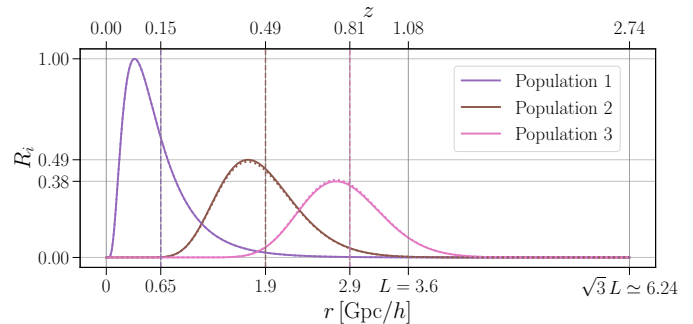


FIG. 4. Radial selection functions modelled as log-normal distributions in redshift (upper x axis) for the three mock galaxy populations. In the figure, the distributions are represented with respect to comoving distances (lower x axis) using the redshift-distance relation. The continuous lines represent the selection functions for the well-specified Model A, while the dotted lines represent the misspecified Model B, both defined by the values provided in Table VI. The small, percent-order difference between Models A and B renders the dotted curves nearly indistinguishable from the solid ones. The vertical dashed lines indicate the means of the log-normal distributions.

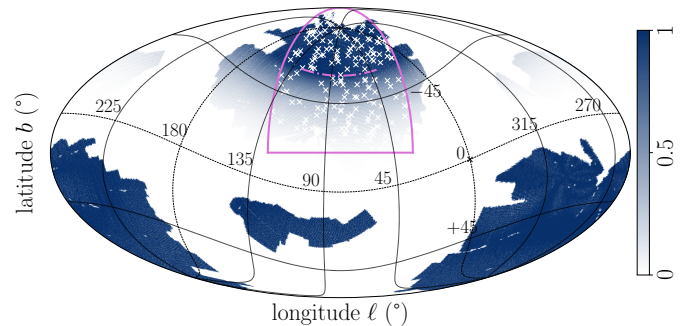


FIG. 5. Survey mask for the well-specified Model A. We added extinction linearly decreasing from 100% at the galactic plane to 0% at 60° galactic latitude (dash-dotted orchid line), along with 256 holes of approximately 0.1-degree radius (white crosses). The observed octant is delineated by the light orchid triangle. The colour scale represents the completeness function $C(\hat{\mathbf{n}})$, with 0 indicating masked regions and 1 indicating unmasked regions, and any value in between indicating partial completeness. In the misspecified Model B, the same mask is used, except for the linear extinction which extends from 0 to 59° galactic latitude.

deviation is defined as $\varsigma_x \equiv \varsigma\sqrt{W_{i,x}}$, where $\varsigma = 1$ is the overall shot noise level. Setting $\bar{N} = 1$ in Equation (37) yields a mean galaxy number density of approximately $6 \times 10^{-3} h^3 \text{Mpc}^{-3}$ for the mock populations of LRGs, which is about an order of magnitude higher than the expected galaxy number density in actual surveys, for instance $5 \times 10^{-4} h^3 \text{Mpc}^{-3}$ in [Berti, Dawson & Dominguez \(2023\)](#). A slice through one realisation of the galaxy

counts fields \mathbf{N}^{g_i} for each population g_i is shown in Figure 3.

E. Summary statistics

The full data vectors \mathbf{d} , consisting of the three 512^3 -dimensional galaxy count fields, are compressed into a summary statistic believed to contain relevant information about the cosmological parameters. In this study, we use the estimated power spectra of the observed and simulated fields, which is a standard choice in cosmological data analysis that has proven to be a powerful tool for constraining cosmological parameters (e.g. Tegmark *et al.*, 2004; Ross *et al.*, 2013). The transformation from the full data space to the space of observed summaries corresponds to the data compressor \mathcal{C} in the BHM of Figure 2.

For each galaxy population g_i , following Leclercq *et al.* (2019), we define the binned data power spectrum as

$$P^{g_i}(k_r) = \sum_{|\mathbf{k}| \in [k_r \pm \delta r]} \frac{|\widehat{N}_k^{g_i}|^2}{N_{k_r} - 2}, \quad (44)$$

for $k_r - \delta r > 0$, where $\widehat{N}_k^{g_i}$ denotes the discrete Fourier transform of \mathbf{N}^{g_i} . N_{k_r} represents the total number of Fourier modes within the wave number shell around k_r . The -2 term arises from the assumption that the data power spectrum follows an inverse- Γ distribution with shape parameter $N_{k_r}/2$ and scale parameter $|\widehat{N}_k^{g_i}|^2/2$, corresponding to the Jeffreys prior for power spectra (Jasche *et al.*, 2010). The summaries Φ are then defined as the concatenation of the three vectors P^{g_i} , $i = 1, 2, 3$, corresponding to the three galaxy populations.

F. Synthetic observations

The ground truth cosmological parameters $\boldsymbol{\omega}_{\text{gt}}$ are drawn from the Planck 2018 prior (Planck Collaboration, 2020). They are given up to the fourth decimal place in Table VIII. We generate synthetic observations Φ_{O} with the well-specified Model A, using

$$\boldsymbol{\theta}_{\text{gt}} = \mathcal{T}(\boldsymbol{\omega}_{\text{gt}}), \quad (45)$$

as the input initial matter power spectrum, with $\boldsymbol{\omega}_{\text{gt}}$ given in Table VIII, whilst fixing $\mathbf{o} = \boldsymbol{\omega}_{\text{gt}}$ in the simulator. The synthetic observations are therefore obtained as

$$\Phi_{\text{O}} | \boldsymbol{\omega}_{\text{gt}} \curvearrowright \int \delta^{\text{D}}(\mathcal{B}(\boldsymbol{\theta}_{\text{gt}}, \boldsymbol{\omega}_{\text{gt}}, \boldsymbol{\psi})) \mathcal{P}(\boldsymbol{\psi}) \, \text{d}\boldsymbol{\psi}. \quad (46)$$

TABLE VIII. Ground truth cosmological parameters.

h	$\Omega_b h^2$	Ω_m	n_s	σ_8
0.6792	0.02247	0.3054	0.9638	0.8210

IV. RESULTS

A. First step: Check for model misspecification

A.1 SELFI posteriors with the well- and misspecified models

We ran $N_0 = 500$ and $N_s \times S = 640$ simulations at and around the expansion point $\boldsymbol{\theta}_0$ defined by Equation (14) and table III to estimate \mathbf{f}_0 and $\nabla_{\boldsymbol{\theta}} \mathbf{f}_0$, respectively. The simulated summaries used for estimating \mathbf{f}_0 , along with their full covariance matrix, are displayed in Figure 6. Using these estimates, we computed the SELFI effective posterior $\mathcal{P}(\boldsymbol{\theta} | \Phi_{\text{O}})$ based on Equations (20) and (21). From the simulated summaries and their covariance matrices alone, it is difficult to distinguish the well- and misspecified models, let alone identify the source of misspecification in Model B. More insight can be gained by examining the SELFI posteriors.

The posterior initial matter power spectrum inferred with the well-specified Model A is represented in green in Figure 7. It is compatible with the truth across all scales, demonstrating the self-consistency of the SELFI assumptions. We further verify that this holds true for a wide range of observed data vectors derived from different sets of cosmological parameters, confirming the unbiasedness of the method (Appendix C 1). The posterior obtained with the misspecified Model B, in red in Figure 7, is implausible: it exhibits an excess of power of about $\sim 2\sigma$ with respect to the prior mean at the largest scales and a lack of power of similar amplitude at the smallest scales, where non-linear physics dominate.

As a quantitative check, Figure 8 depicts the Mahalanobis distances between $\mathcal{P}(\boldsymbol{\theta})$ and the reconstructed mean power spectra $\boldsymbol{\gamma}$ for each model, computed using Equation (24), in comparison to those between $\mathcal{P}(\boldsymbol{\theta})$ and 5 000 random samples $\boldsymbol{\theta}_n = \mathcal{T}(\boldsymbol{\omega}_n)$. Each $\boldsymbol{\omega}_n$ is drawn from the prior $\mathcal{P}(\boldsymbol{\omega})$ on the cosmological parameters. The Mahalanobis distances are multivariate analogues of the standard scores, accounting for correlations between the components, and measure the deviation of the reconstructions from the prior distribution. Large deviations suggest significant disagreement, prompting further investigation. We found that the distance for Model A, $d_{\text{M}}(\boldsymbol{\gamma}_{\text{A}}, \boldsymbol{\theta}_0 | \mathbf{S}) = 1.816$, is much smaller than the distance for Model B, $d_{\text{M}}(\boldsymbol{\gamma}_{\text{B}}, \boldsymbol{\theta}_0 | \mathbf{S}) = 2.827$. A larger distance does not necessarily imply a worse model, but hints at the presence of systematic effects. For comparison, the mean Mahalanobis distance from $\mathcal{P}(\boldsymbol{\theta})$ to the 5 000 $\boldsymbol{\theta}_n$ samples is $\langle d_{\text{M}}(\boldsymbol{\theta}_n, \boldsymbol{\theta}_0 | \mathbf{S}) \rangle_n = 2.431$. The disagreement between $d_{\text{M}}(\boldsymbol{\gamma}_{\text{B}}, \boldsymbol{\theta}_0 | \mathbf{S})$ and the value typically observed from random samples, $\langle d_{\text{M}}(\boldsymbol{\theta}_n, \boldsymbol{\theta}_0 | \mathbf{S}) \rangle_n$, highlights how percent-

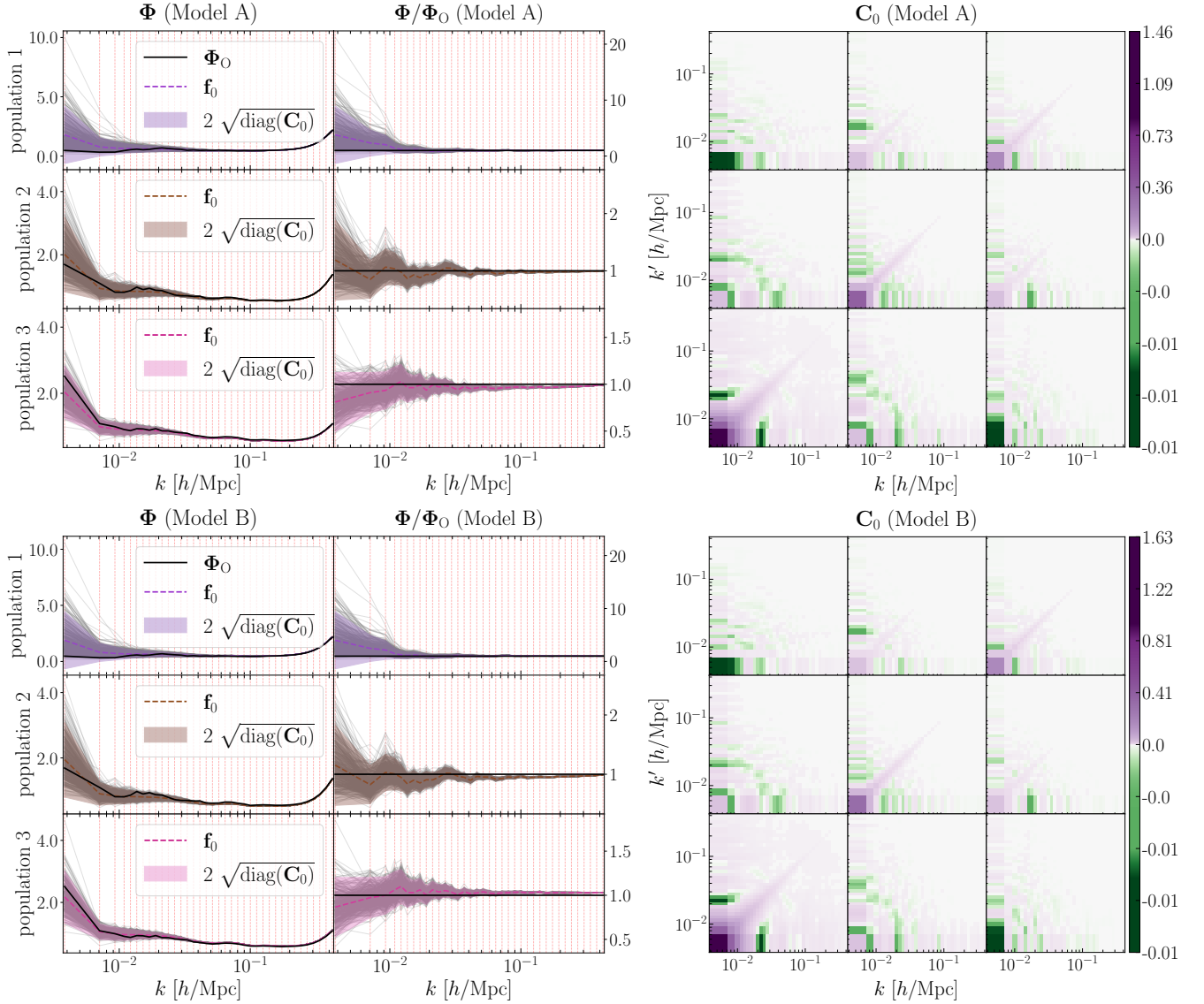


FIG. 6. Data intervening in the computation of the SELFI posterior. (Left panels) Observed and simulated summary statistics for Model A (*well-specified; upper panel*) and B (*misspecified; lower panel*). For each population, the simulated summaries are shown in grey and their means are represented as dotted coloured lines. The shaded areas correspond to $\pm 2\sigma$ around their mean. The solid black line corresponds to the observations Φ_O . The binning is indicated by the vertical dashed lines. (Right panels) Covariance matrices for Models A and B. For each (k, k') entry, the colour scale represents the covariance between the k -th and k' -th modes. The diagonal blocs of the full covariance matrix correspond to the intra-population covariance; the extra-diagonal blocs correspond to the inter-populations covariances.

order variations in the modelling assumptions strongly influence the reconstruction of the initial matter power spectrum θ , pulling it away from the prior. This motivates a careful investigation of systematic effects, which we undertake in the following sections.

Additionally, since the prior given by Equation (9) embeds substantial information about the functional shape of the initial matter power spectrum, one might question how the SELFI algorithm performs with a less informative prior. [Leclercq et al. \(2019\)](#) demonstrated that a wigglerless prior centred on $\theta_0 \equiv \mathbf{1}_{\mathbb{R}^S}$ enables precise recovery

of initial features such as the BAOs up to mildly non-linear scales. Given the enhanced complexity of the data model employed here—incorporating extinction, point-source contamination, and radial selection effects, whilst using a lower mass-resolution—we successfully verified that the BAOs are still retrievable in this set-up using a prior agnostic to the BAOs, as is shown in Appendix C 2.

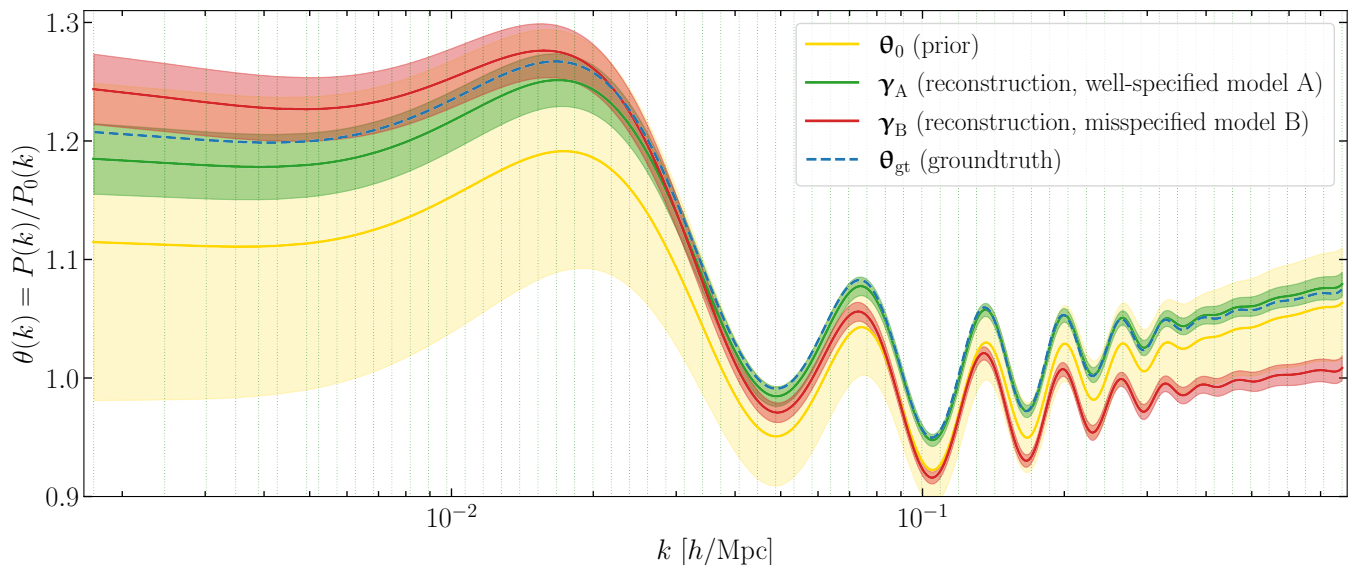


FIG. 7. Prior and SELFI posteriors for the initial matter power spectrum θ given the observations Φ_{O} . The ground truth θ_{gt} is indicated by the dashed blue line. The prior and posterior means, θ_0 , γ_{A} and γ_{B} , are represented respectively by the yellow, green and red lines, along with their 2σ credible regions (shaded yellow, green, and red areas). The vertical dashed lines indicate the support wave numbers for the initial matter power spectrum representation. The posterior obtained with the well-specified Model A is unbiased over all scales, whilst the posterior obtained with the misspecified Model B exhibits an excess and a lack of power at the largest and smallest scales, respectively.

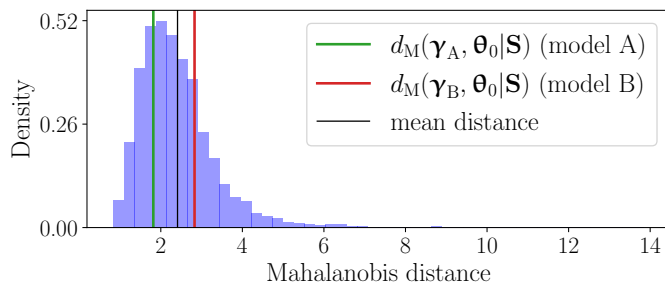


FIG. 8. Histogram of the Mahalanobis distances $d_{\text{M}}(\theta_n, \theta_0|\mathbf{S})$ between the prior and 5000 power spectra $\theta_n \equiv \mathcal{T}(\omega_n)$ sampled from Equation (6). The mean value is indicated by the vertical solid black line. The green and red lines indicate the distances from γ_{A} and γ_{B} to the prior, respectively.

A.2 Impact of galaxy biases on the initial power spectrum reconstruction

Due to the non-linearity of the data model, the impact of the bias model on the posterior is in general out of reach of theoretical considerations. Linear galaxy biases, however, are expected to have a mostly scale-independent effect on the SELFI reconstruction γ of the initial matter power spectrum, as demonstrated in Appendix D based on qualitative considerations. This effect is observed on Figure 9a, which illustrates the impact of the linear galaxy bias parameters on the SELFI posterior distribu-

tion for the initial matter power spectrum. We considered a constant relative error in the $\pm 2\%$ range for the linear galaxy bias parameters of the three populations, as indicated by the colour scale. All scales experience a similar shift in standard deviations, which is consistent with the analytical expectations.

This demonstrates the ability of our framework to accurately diagnose the impact of systematic effects using the reconstructed initial matter power spectrum. We retrieve that the effect of misspecified linear galaxy bias parameters closely resembles a simple rescaling of the initial matter power spectrum by a constant factor, highlighting the well-known degeneracy between the linear galaxy bias parameters and the value of σ_8 (Beutler *et al.*, 2012; Arnalte-Mur *et al.*, 2016; Desjacques, Jeong & Schmidt, 2018; Repp & Szapudi, 2020).

A.3 Impact of linear extinction, selection functions, punctual contaminations, and inaccurate redshifts

Even when the internal mechanisms of the forward model are known and well understood, assessing how a particular systematic effect influences the reconstruction solely through analytical considerations is often impractical. If an analytical expression can be derived, it may not be accurate due to correlations with other systematic effects, and its validity is likely to depend on the specificities of the hidden-box forward model. In such cases, we show that our framework makes it possible to con-

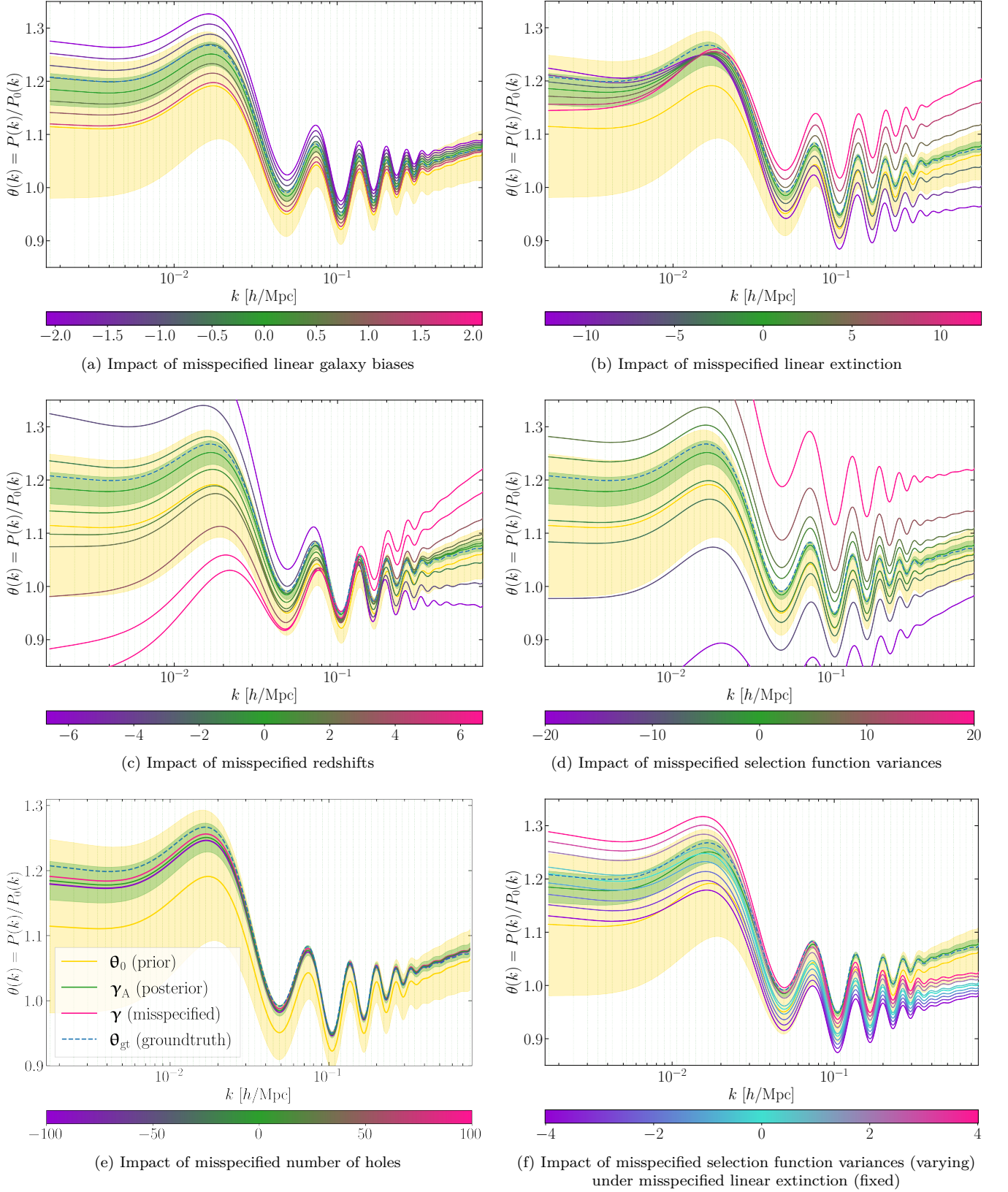


FIG. 9. Ensemble of SELFIE posteriors for the initial matter power spectrum θ conditional on the observed data Φ_{O} for different observational models, used to diagnose systematic effects. All the posteriors are derived from a single, common set of N -body simulations. They make it possible to disentangle individual systematic contributions by comparing their differential impact

FIG. 9. **Continued.** across the range of wave numbers spanned by the power spectra. The colour scales indicate the relative error associated with the systematic effects considered in each sub-figure. The solid yellow line denotes the prior mean θ_0 and the ground truth θ_{gt} is indicated by the dashed blue line. The vertical dashed lines indicate the support wave numbers for the initial matter power spectrum representation. The 2σ credible regions for the prior and the posterior with the well-specified Model A correspond to the shaded yellow and green areas, respectively. The posterior means γ are represented by the coloured continuous lines for varying degrees of misspecification. For clarity, their corresponding credible regions have been omitted.

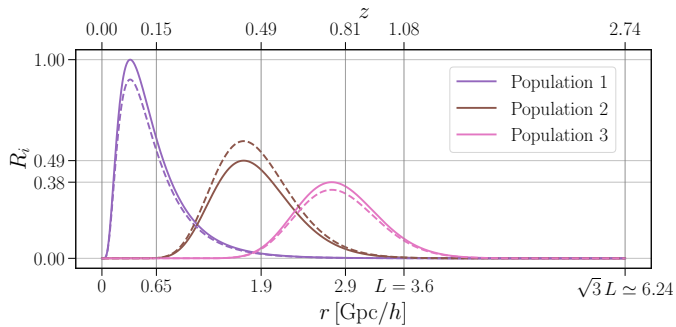


FIG. 10. Profiles of the well- and misspecified selection functions R_i for the three mock galaxy populations. The continuous lines represent the selection functions used in Model A. The dashed lines are derived by underestimating $n_{1,2}(z)$ by 10% whilst maintaining $n_{\text{tot}}(z)$ constant.

duct a thorough numerical investigation by reconstructing γ with Equation (20), whilst varying the values of the parameters involved in the model of the systematic effect. As a demonstration, we examine the impact of misspecified extinction near the galactic plane, misspecified selection functions, inaccurate redshifts, and punctual contaminations. All these numerical investigations rely on the same, common set of N -body simulations previously computed to obtain the posterior with Model A and already used to evaluate the effect of linear galaxy bias parameters in Section IV A 2.

Figure 9b illustrates the effect of over- or underestimating the amount of extinction near the galactic plane. The colour scale represents the relative mean visibility between the misspecified and well-specified models, averaged over the three-dimensional survey window function. The extinction reduces the amplitude of small scales correlations; thus, overestimating extinction in the misspecified mask leads to a power deficit at small scales in the simulated summaries, shifting the reconstructed spectrum upwards. Conversely, underestimating extinction shifts the reconstructed spectrum downwards at small scales. At larger scales, excessive extinction in the misspecified mask introduces spurious fluctuations which are not retrieved in the observations, adding power to the largest k -modes and pushing the reconstruction downwards. As is shown in Figure 9b, the transition between these two regimes occurs at a constant scale, regardless of the degree of error in the extinction. This characteristic scale provides a means to distinguish the effects of extinction from other sources of systematic errors.

We emulated a systematic effect analogous to inaccurate redshifts due to line interlopers (e.g. Pullen *et al.*, 2016; Addison *et al.*, 2019; Massara *et al.*, 2021) by increasing (or decreasing) the observed density of the central spectroscopic galaxy bin whilst correspondingly decreasing (or increasing) the densities of the two other populations, ensuring that the total density remained unchanged. An example of the resulting misspecified radial selection functions is shown in Figure 10. The resulting reconstructions, displayed in Figure 9c, demonstrate that even small, percent-level variations significantly affect the posterior on the initial matter power spectrum.

Figure 9d shows the impact of another source of systematic error associated with selection functions, specifically the impact of misspecified variances in the radial log-normal distributions. The result is comparable to that of misspecified galaxy bias parameters, though it is slightly more pronounced at smaller scales.

In complex data models displaying multiple putative sources of systematic effects alongside potentially many corresponding model parameters, it is crucial to know which effects are most likely to have a significant impact on the initial matter power spectrum, and should be prioritised for further investigation. Notably, some systematic effects may have a negligible impact on the initial matter power spectrum. Figure 9e illustrates the effect of misspecifying the number of holes in the survey mask in our set-up, using 0, 256, or all 512 holes defined at the beginning of the study, which represent the masking of bright stars or other point sources of contamination expected in cosmological surveys. The reconstruction appears largely unaffected by the number of holes, as their small angular size causes them to be overwhelmed by small-scale noise.

A.4 Joint impact of multiple systematic effects

Naturally, one is not restricted to studying individual systematic effects in isolation, and the SELFIE posterior can be employed to explore how jointly misspecified observational effects influence the reconstructed initial matter power spectrum. This approach would be particularly beneficial for designing the data model of a real survey, enabling the assessment of the joint impact of different systematic effects on the cosmological inference whilst accounting for potential correlations between them. For example, Figure 9f shows the combined impact on the initial matter power spectrum of misspecified variances in the log-normal selection functions alongside incorrectly

specified linear extinction.

Conversely, if a comprehensive study of multiple individual systematic effects has already been conducted, one can use it to disentangle their contributions when faced with a surprising posterior that warrants further investigation. For instance, if we obtain one of the reconstructions shown in Figure 9f, assuming unknown additive contributions of the five effects described in Section IV A 3, we can easily disentangle individual contributions as follows. Shifting the reconstruction until it aligns with one of the characteristic scales associated with misspecified extinction or redshifts, we deduce that the systematic error most consistent with the observed reconstruction is a -10% error in the extinction, along with the corresponding error in the variance of the selection functions. As the model complexity increases, greater caution is required when interpreting the results, since multiple systematic effects can have degenerate impacts on the reconstructed power spectra. This underscores the importance of thoroughly investigating the influence of each individual systematic effect beforehand.

If known and unknown systematic effects are entangled, it remains possible to first identify the former using the characterisation presented in Figure 9. Running the framework while accounting for all known sources of systematic effects ensures that only unknown systematic effects and/or new physics remain to be characterised in the inferred initial matter power spectrum. Consequently, our framework has significant potential for detecting previously unknown systematic effects. This approach is conceptually distinct from that introduced by Porqueres *et al.* (2019), who identify and marginalise over unknown systematic effects within explicit likelihood inference.

A.5 Impact of the gravity solver

The gravity solver is a critical component of the data model. There is some flexibility in selecting the total number of time steps n_{steps} , dark matter particles N_{p} , and the resolution of the particle-mesh grid used to compute the gravitational forces. Often, a trade-off must be made between the numerical cost of the resolution and the precision required by the observations and scientific objectives. The standard approach is to specify a target precision for the first or second-order statistics of the final dark matter overdensity fields and adjust the gravity solver parameters accordingly, based on convergence tests or comparisons with higher resolution simulations.

Unlike the systematic effects discussed in Sections IV A 2 to IV A 4, obtaining multiple posteriors on the initial matter power spectrum for various configurations of the gravity solver implemented in the forward model requires re-running N -body simulations. However, the numerical cost of obtaining a single SELFI posterior for the initial matter power spectrum— $\mathcal{O}(10^3)$ N -body simulations in this study—remains orders of magnitude

lower than for the cosmological parameters— $\mathcal{O}(10^5)$ N -body simulations in this study. Consequently, our framework presents further value for investigating the error caused by misspecified gravity models on the posterior initial matter power spectrum. Similarly, our framework could be employed to diagnose the effect of baryons in the hidden-box model based on the inferred initial matter power spectrum, provided one is willing to incur the numerical cost of incorporating baryonic physics into the simulator.

We refer to the error on the reconstructed initial matter power spectrum as the inverse error, as opposed to the direct error on the measured galaxy power spectra. We show that measuring this inverse error is particularly relevant for large-scale galaxy surveys: it highlights the sensitivity of the inference to the gravity solver parameters, which is not apparent from the direct error on the galaxy count fields.

Figures 11a and 11b illustrate the effect of using 10 instead of 20 time steps for the gravitational evolution with COLA. Whilst the direct error in the measured galaxy power spectra compared to Model A remains below 1% across all scales, the inverse error in the SELFI posterior exceeds 2% for $k \leq 4 \cdot 10^{-3}$. This discrepancy arises due to the non-linearity of the inversion: small differences in the predicted galaxy power spectra between Models A and B can propagate into substantial biases in the posteriors after solving the inverse problem. As is shown in Figure 11b, the posterior rejects the ground truth by more than 2σ across most scales. The SELFI posterior is therefore highly sensitive to the time-stepping in the gravity solver. To achieve, for example, a 1% precision on the posterior, it is necessary to ensure an even higher precision in the galaxy count power spectra.

Similarly, Figures 11c and 11d highlight the importance of accounting for light cone effects in the forward model: the SELFI posterior consistently rejects the ground truth when all three galaxy populations are defined from the snapshot at redshift $z_1 = 0.15$, compared to using z_1 , z_2 , and z_3 in Model A. Since the cosmological structure is less evolved at higher redshifts, this results in overestimating the measured power spectrum amplitude for the two most distant galaxy populations, which pushes the SELFI posterior downwards at all scales. We note that this effect is highly degenerate with that of misspecified galaxy biases. Both risk biasing the value of σ_3 inferred from the data if not properly accounted for.

Strikingly, Figures 11e and 11f show that using 2LPT instead of COLA in the forward model significantly biases the posterior on the initial matter power spectrum. This arises because the range of scales considered in this study extends well beyond $k_{\text{lin}} \simeq 0.15 h/\text{Mpc}$, commonly considered as the smallest scale of the linear regime (e.g. Colless *et al.*, 2001), up to $k_{\text{max}} \simeq 0.4 h/\text{Mpc}$. Within the SELFI framework, all scales are coupled by the non-linearity. Over-prediction of small-scale power by 2LPT (due to the mass resolution) results in under-prediction of large scale power to fit the data. Furthermore, since

the number of small-scale modes vastly exceeds that of large-scale modes, the posterior computation sacrifices large scale accuracy to fit small scales. The forward error on the galaxy count power spectra reaches $\sim 7\%$ at the smallest scales, and the SELFI posterior rejects the ground truth by almost 2σ across most scales. This underscores the necessity of employing fully non-linear gravity solvers to accurately extract small-scale information from large-scale galaxy surveys.

B. Second step: Cosmological parameters

After checking for model misspecification, the second step of the framework consists of inferring the target cosmological parameters, $\boldsymbol{\omega}$, given the compressed summaries $\tilde{\boldsymbol{\omega}}_O$. For score compression, we re-used the estimates \mathbf{f}_0 and $\nabla_{\boldsymbol{\theta}}\mathbf{f}_0$ computed in the first step, and estimate the gradient $\nabla\mathcal{T}$ of CLASS at the fiducial cosmological parameters $\tilde{\boldsymbol{\omega}}_0$ using fifth order finite differences. To perform the inference, we use the ELFI package (Lintusaari *et al.*, 2018), which implements the variant of ABC-PMC proposed by Simola *et al.* (2021) and discussed in Section II C 2.

To reduce computational costs, in this study, we inferred only Ω_m , Ω_b , n_S , and σ_8 whilst fixing h to the ground truth given in Table VIII. This choice was further motivated by the fact that our data model carries no additional information beyond the prior concerning the value of h . For practical purposes, we used nine distinct ABC-PMC populations of 64 particles each, aggregating the $J = 576$ final samples and corresponding weights to obtain a posterior distribution of $(\Omega_m, \Omega_b, \sigma_8, n_S)$. Figure 12 shows the posteriors obtained using a kernel density estimate with the J weighted accepted samples. The shaded yellow area corresponds to 2σ credible contours on the prior. The posterior with the well-specified Model A is shown in green; it is unbiased for all cosmological parameters.

Replacing the accurate data Model A with the misspecified Model B for ABC-PMC yields the posterior in red. This substitution results in over-concentrating the posterior distributions of σ_8 , Ω_m , and n_S , and introduces a bias exceeding 2σ in the (σ_8, Ω_m) plane. The bias in the marginal posterior of σ_8 is to be expected in light of the well-known degeneracy between σ_8 and galaxy bias parameters (Beutler *et al.*, 2012; Arnalte-Mur *et al.*, 2016; Desjacques, Jeong & Schmidt, 2018; Repp & Szapudi, 2020).

V. DISCUSSION AND CONCLUSION

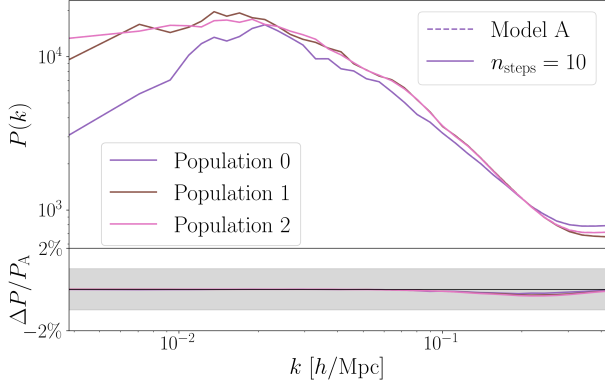
We have presented a method for thoroughly assessing individual or combined systematic effects in galaxy surveys using the initial matter power spectrum. We provide a practical guide for evaluating the impact of various systematic effects, demonstrated using a spectroscopic

galaxy survey model through a quantitative assessment of the effect of misspecified linear galaxy biases, extinction near the galactic plane, selection functions, punctual contaminations, inaccurate redshifts, and imprecise gravity solver.

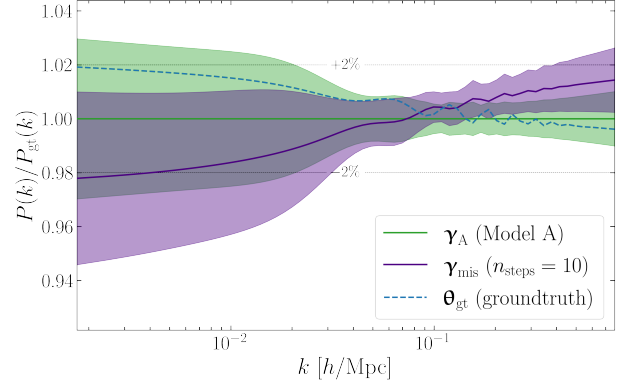
The method introduced in this study offers a Bayesian framework for addressing model misspecification in field-based implicit-likelihood cosmological inference. Notably, we have shown that even small, percent-level errors can significantly skew cosmological inferences derived from galaxy clustering probes. This was illustrated by a bias exceeding 2σ in the (σ_8, Ω_m) plane (Figure 12), which we were able to detect and correct (Figures 7 and 9) prior to inferring the cosmological parameters. Correct identification of systematic effects is crucial for accurately measuring primordial features of the Universe, such as non-Gaussianities—a major scientific goal of next-generation galaxy surveys (Andrews *et al.*, 2023). Our method could serve as a critical tool for field-based ILI of these primordial features.

Our approach primarily centres on systematic effects that influence the initial matter power spectrum reconstruction. While we have assumed that the inferred spectrum serves as a reliable proxy for cosmological parameters, there may be systematic effects that do not affect the initial matter power spectrum yet still introduce biases in cosmological inferences. Such effects fall outside the current scope of this framework. In this paper, we assumed fixed deterministic linear galaxy bias parameters, but scale-dependent or non-linear bias models could be incorporated within the same framework. Addressing model misspecification for more sophisticated bias models would be particularly relevant for the inference of primordial non-Gaussianities. If a prior distribution of the bias values is available, they can be treated as additional nuisance parameters alongside $\boldsymbol{\psi}$ and marginalised over without altering the statistical framework presented here. Alternatively, they could be treated as additional input parameters alongside $\boldsymbol{\theta}$ and inferred jointly with the initial matter power spectrum. These avenues remain for future investigation.

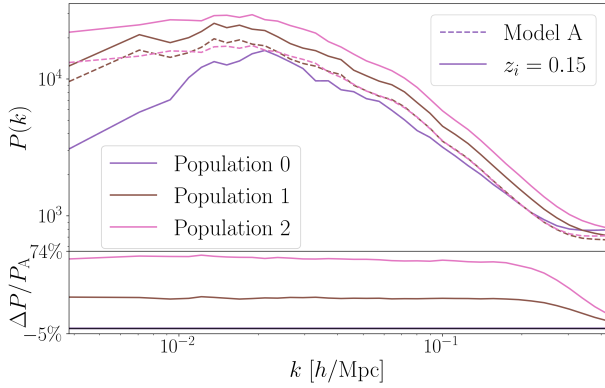
Potential extensions of the method include incorporating higher-order summary statistics from the full galaxy count fields into the inference (Gil-Marín *et al.*, 2015; Philcox & Ivanov, 2022), which provide valuable information, for instance for constraining dark energy (Fazolo, Amendola & Velten, 2022). Other options include using wavelet scattering transform coefficients (Régald-Saint Blancard *et al.*, 2024), and additional cosmological probes such as peculiar velocity tracers (Prideaux-Ghee *et al.*, 2023). The compression step could be improved by using information-maximising neural networks (Charnock, Lavaux & Wandelt, 2018; Mäkinen *et al.*, 2024; Lanzieri *et al.*, 2024), which complement physically motivated summary statistics. These beyond 2-pt approaches are particularly relevant for extracting the maximum amount of information from upcoming galaxy surveys and could reveal additional sources of systematic



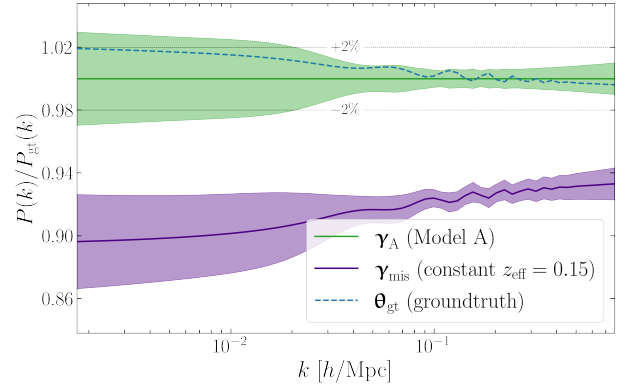
(a) Galaxy power spectra with $n_{\text{steps}} = 10$ compared to $n_{\text{steps}} = 20$ for Model A (P_A)



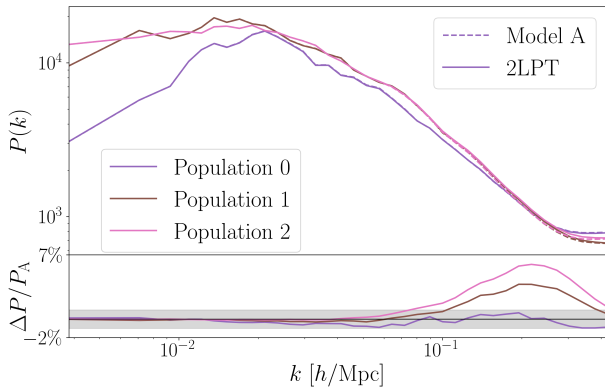
(b) The SELFI posterior with $n_{\text{steps}} = 10, 20$



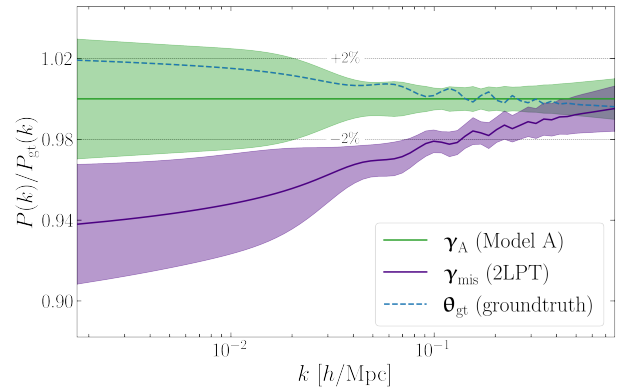
(c) Galaxy power spectra with (P_A) and without light cone



(d) The SELFI posterior with or without light cone



(e) Galaxy with 2LPT instead of N -body (P_A)



(f) The SELFI posterior with 2LPT or N -body

FIG. 11. Impact of the gravity solver parameters on the SELFI posterior. Panels (a, c, e) display the summary statistics Φ for the three galaxy count fields, comparing the well-specified Model A (dashed lines) with the misspecified model (solid lines). The lower parts of these panels show the relative error between the two models, with shaded regions corresponding to a 1% error margin. Panels (b, d, f) show the corresponding SELFI posteriors for the initial matter power spectrum θ , with the well-specified and misspecified models represented by green and indigo lines, respectively. (a) Example of summary statistics for a single realisation with $n_{\text{steps}} = 10$ (solid lines) as opposed to $n_{\text{steps}} = 20$ time steps for Model A (dashed lines) in the gravitational evolution with COLA. Although the direct error remains well below 1% across all scales, the inverse error on the SELFI posterior (b) reaches 2% at the largest scales, corresponding to a deviation greater than 1σ from the well-specified Model A. (c) Summary statistics using only the final snapshot at redshift $z_1 = 0.15$ for the three mock galaxy populations, thereby neglecting light cone effects (solid lines). The forward error reaches 74% at the largest scales for the most distant galaxy population, and the corresponding SELFI posterior (d) significantly rejects the ground truth across all scales. (e) Summary statistics using a pure 2LPT gravity model instead of N -body simulations to define the galaxy populations (solid lines). The forward error reaches $\sim 7\%$ at the smallest scale, and the ground truth is significantly rejected by the SELFI posterior (f), which deviates by more than 2σ compared to Model A at the largest scales.

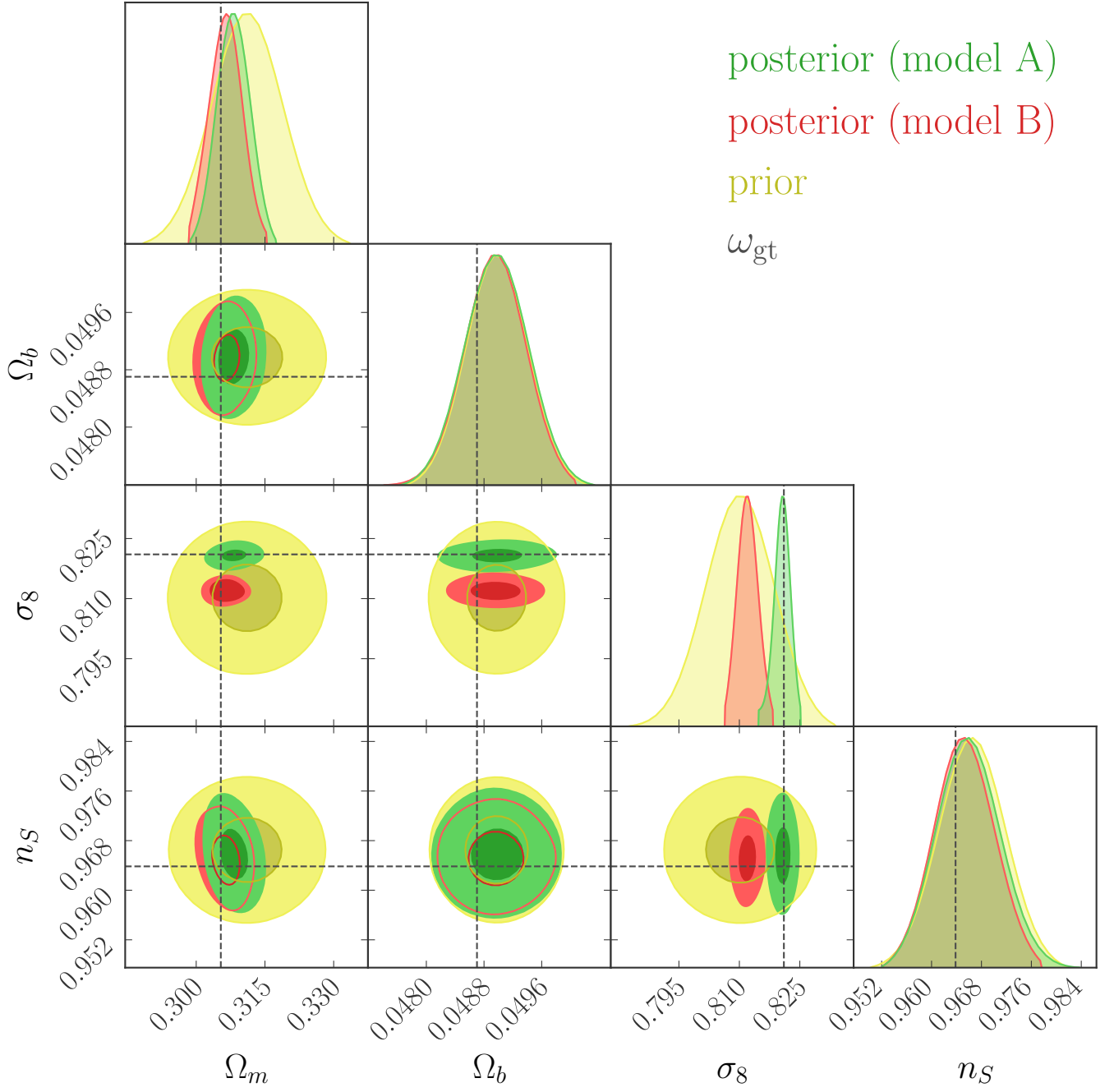


FIG. 12. Prior $\mathcal{P}(\boldsymbol{\omega})$ (yellow) and posterior $\mathcal{P}(\boldsymbol{\omega}|\tilde{\boldsymbol{\omega}}_O)$ distributions of $(\Omega_m, \Omega_b, \sigma_8, n_S)$, estimated using Population Monte Carlo based on the Fisher-Rao distance $d_{\text{FR}}(\tilde{\boldsymbol{\omega}}, \tilde{\boldsymbol{\omega}}_O)$ between simulated and observed summaries. The posterior with the well-specified Model A is represented by the green contours, whilst the red contours show the results with the misspecified Model B, both depicting the 1σ and 2σ credible regions. The percent-level misspecification in Model B introduces a bias exceeding 2σ in the (Ω_m, σ_8) plane. The one-dimensional marginal posterior distributions of the parameters are displayed on the diagonal, following the same colour scheme. The dashed line indicates the ground truth parameters $\boldsymbol{\omega}_{\text{gt}}$.

effects which should be accounted for in cosmological inferences based on these summaries (*Beyond-2pt Collaboration, 2024*).

In conclusion, we have proposed a method to address the issue of model misspecification in implicit likelihood, field-based cosmological inferences. It enables a comprehensive investigation of both simulation- and observation-related systematic effects in galaxy surveys, leveraging both theoretical insights and prior knowledge of the initial matter power spectrum. We demonstrated the effectiveness of this method by quantifying the impact of various systematic effects on the inferred initial matter power spectrum. Furthermore, we emphasised the importance of using an accurate model for gravitational evolution within the hidden-box model: our results indicate that pure 2LPT is insufficient for the range of scales considered in this study, which is $k \in [1.75 \times 10^{-3}, 4.47 \times 10^{-1}] h/\text{Mpc}$. Our framework can be used with any hidden-box model of galaxy surveys developed for cosmological inference pipelines, making it a versatile tool for addressing model misspecification in cosmological data analysis. It has the potential to significantly enhance the robustness of cosmological inferences from upcoming galaxy surveys such as DESI, *Euclid*, and LSST, for which the complexity of data models and the number of systematic effects will be substantial.

CODE AVAILABILITY

This study relies on the pySELFIE implementation of the SELFIE (*Leclercq et al., 2019*) algorithm, which is publicly available at pyselfie.florent-leclercq.eu. The gravitational evolution is performed using a modified version of the publicly available SIMBELMYNE cosmological solver (bitbucket.org/florent-leclercq/simbelmyne, *Leclercq, Jasche & Wandelt, 2015*). The code and data underlying this paper, including the hidden-box model of galaxy surveys described in the article and routines to perform the inference using our framework in a cluster environment, are publicly available at github.com/hoellin/selfisys_public.

A. CONVERGENCE OF THE POSTERIOR

Considerations about the degrees of freedom in the estimated covariance matrix given by Equation (13) impose the required number of simulations at the expansion point to be at least $N_0 \geq P + 3 = 114$. However, the convergence may require more simulations depending for instance on the observational noise level. We checked based on the evolution of the spectral and Frobenius norms of \mathbf{C}_0 that sufficient convergence was reached after $\simeq 450$ simulations (see Figure 13), and we fixed the number of simulations at the expansion point to linearise the hidden-box to $N_0 = 500$. We also verified that using in between $\simeq 350$ and $\simeq 500$ simulations yielded vanish-

ing differences in the corresponding initial matter power spectrum posteriors.

Similarly, we ensured sufficient convergence for the gradients by looking at the evolution of $(\nabla \mathbf{f}_0)^\top \mathbf{C}_0^{-1} \nabla \mathbf{f}_0$ where \mathbf{C}_0 was estimated using all the $N_0 = 500$ simulations available at the expansion point. We fixed $N_S = 10$ to obtain the SELFIE posteriors presented in this article, and checked using Model A that restricting to any number of simulations between 2 and 30 per directional derivative yielded negligible difference in the posterior.

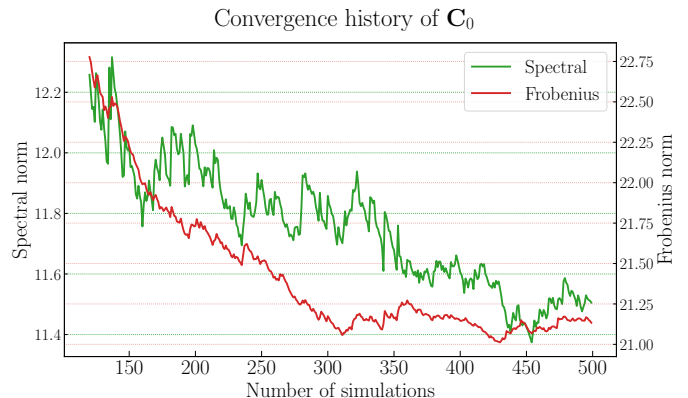


FIG. 13. Convergence history of the covariance. We used the correlation matrix rather than \mathbf{C}_0 to compute the norms.

B. EFFECTIVE POSTERIOR FOR THE INITIAL MATTER POWER SPECTRUM WHEN THE PRIOR MEAN DIFFERS FROM THE EXPANSION POINT

We generalise the derivation of the SELFIE equations from *Leclercq et al. (2019)*, to the case where the prior mean $\hat{\boldsymbol{\theta}}_\omega$ differs from the expansion point $\boldsymbol{\theta}_0$. The SELFIE effective log-likelihood given by Equation (18) can be rewritten in canonical form as

$$-2\hat{\ell}_\theta^{N_0}(\boldsymbol{\theta}) = \log |2\pi \mathbf{C}_0| + \boldsymbol{\mu}_0^\top \mathbf{N}_0 \boldsymbol{\mu}_0 - 2\boldsymbol{\mu}_0^\top \boldsymbol{\theta} + \boldsymbol{\theta}^\top \mathbf{N}_0^{-1} \boldsymbol{\theta}, \quad (\text{B1})$$

with $\boldsymbol{\mu}_0 \equiv \mathbf{N}_0^{-1} \mathbf{y}_0 = \mathbf{N}_0^{-1} \boldsymbol{\theta}_0 + (\nabla \mathbf{f}_0)^\top \mathbf{C}_0^{-1} (\boldsymbol{\Phi}_O - \mathbf{f}_0)$, where we have defined

$$\begin{aligned} \mathbf{N}_0 &\equiv [(\nabla \mathbf{f}_0)^\top \mathbf{C}_0^{-1} \nabla \mathbf{f}_0]^{-1}, \\ \mathbf{y}_0 &\equiv \boldsymbol{\theta}_0 + (\nabla \mathbf{f}_0)^{-1} \cdot (\boldsymbol{\Phi}_O - \mathbf{f}_0). \end{aligned} \quad (\text{B2})$$

Similarly, the prior given by Equation (7) can be written

$$-2 \log \mathcal{P}(\boldsymbol{\theta}) = \log |2\pi \mathbf{S}| + \boldsymbol{\eta}^\top \mathbf{S} \boldsymbol{\eta} - 2\boldsymbol{\eta}^\top \boldsymbol{\theta} + \boldsymbol{\theta}^\top \mathbf{S}^{-1} \boldsymbol{\theta} \quad (\text{B3})$$

in canonical form, where $\boldsymbol{\eta} \equiv \mathbf{S}^{-1} \hat{\boldsymbol{\theta}}_\omega$. The effective posterior therefore verifies

$$\begin{aligned} -2 \log \mathcal{P}(\boldsymbol{\theta} | \boldsymbol{\Phi}_O) &= -2\hat{\ell}_\theta^{N_0}(\boldsymbol{\theta}) - 2 \log \mathcal{P}(\boldsymbol{\theta}) \\ &= -2(\boldsymbol{\mu}_0 + \boldsymbol{\eta})^\top \boldsymbol{\theta} + \boldsymbol{\theta}^\top (\mathbf{N}_0^{-1} + \mathbf{S}^{-1}) \boldsymbol{\theta} \\ &\quad + \text{constant terms}, \end{aligned} \quad (\text{B4})$$

where we recognise the canonical form of a Gaussian distribution with covariance matrix

$$\mathbf{\Gamma} \equiv (\mathbf{N}_0^{-1} + \mathbf{S}^{-1})^{-1} = [(\nabla \mathbf{f}_0)^\top \mathbf{C}_0^{-1} \nabla \mathbf{f}_0 + \mathbf{S}^{-1}]^{-1}, \quad (\text{B5})$$

and mean

$$\begin{aligned} \boldsymbol{\gamma} &\equiv \mathbf{\Gamma}(\boldsymbol{\mu}_0 + \boldsymbol{\eta}) \\ &= \mathbf{\Gamma} [(\nabla \mathbf{f}_0)^\top \mathbf{C}_0^{-1} \nabla \mathbf{f}_0 \boldsymbol{\theta}_0 + (\nabla \mathbf{f}_0)^\top \mathbf{C}_0^{-1} \nabla \mathbf{f}_0 (\nabla \mathbf{f}_0)^{-1} \\ &\quad \cdot (\boldsymbol{\Phi}_O - \mathbf{f}_0) + \mathbf{S}^{-1} \hat{\boldsymbol{\theta}}_\omega] \\ &= \mathbf{\Gamma} \{ [(\nabla \mathbf{f}_0)^\top \mathbf{C}_0^{-1} \nabla \mathbf{f}_0 + \mathbf{S}^{-1}] \boldsymbol{\theta}_0 - \mathbf{S}^{-1} \boldsymbol{\theta}_0 \\ &\quad + (\nabla \mathbf{f}_0)^\top \mathbf{C}_0^{-1} \cdot (\boldsymbol{\Phi}_O - \mathbf{f}_0) + \mathbf{S}^{-1} \hat{\boldsymbol{\theta}}_\omega \} \\ &= \boldsymbol{\theta}_0 + \mathbf{\Gamma} \mathbf{S}^{-1} \boldsymbol{\Delta} + \mathbf{\Gamma} (\nabla \mathbf{f}_0)^\top \mathbf{C}_0^{-1} \cdot (\boldsymbol{\Phi}_O - \mathbf{f}_0), \quad (\text{B6}) \end{aligned}$$

where $\boldsymbol{\Delta} \equiv (\boldsymbol{\theta}_0 - \hat{\boldsymbol{\theta}}_\omega)$, giving Equation (21).

C. CONSISTENCY CHECKS

1. Unbiasedness of the posterior initial power spectrum

To consistently assess the unbiasedness of the method, we sampled ten different ground truth set of cosmological parameters from the prior, computed the corresponding observed vector $\boldsymbol{\Phi}_O$ for each case, and confirmed both visually and quantitatively that the resulting SELFIE posterior remained consistently unbiased. This demonstrates the robustness of the method with respect to the value of the ground truth cosmological parameters.

2. Inference using a wiggle-less prior

As a consistency check, we verified that SELFIE successfully retrieves the BAOs within the set-up described in this article, even when the prior does not provide any information about the oscillations. We postulate a Gaussian prior given by

$$-2 \log \mathcal{P}(\boldsymbol{\theta}) \equiv \log |2\pi \mathbf{S}| + \|\boldsymbol{\theta} - \boldsymbol{\theta}_0\|_{\mathbf{S}^{-1}}^2, \quad (\text{C1})$$

where the expansion point $\boldsymbol{\theta}_0$ and the covariance matrix \mathbf{S} differ from those of Equation (7). Namely, we set the mean to $\boldsymbol{\theta}_0 \equiv \mathbf{1}_{\mathbb{R}^S}$, corresponding to the BBKS power spectrum for the fiducial cosmological parameters, and, following the procedure described by Leclercq *et al.* (2019), we define the prior covariance matrix as

$$\mathbf{S} \equiv \theta_{\text{norm}}^2 \mathbf{u} \mathbf{u}^\top \circ \mathbf{K}, \quad (\text{C2})$$

where \circ denotes the Hadamard product and \mathbf{K} is a radial basis function defined by

$$(\mathbf{K})_{ss'} \equiv \exp \left[-\frac{1}{2} \left(\frac{k_s - k_{s'}}{k_{\text{corr}}} \right)^2 \right], \quad (\text{C3})$$

and \mathbf{u} is a correction accounting for cosmic variance,

$$(\mathbf{u})_s \equiv 1 + \sigma_s = 1 + \frac{\alpha_{\text{cv}}}{k_s^{3/2}}. \quad (\text{C4})$$

k_{corr} determines the length scale on which power spectrum amplitudes of different wave number correlate with each other. α_{cv} characterises the ‘‘strength’’ of cosmic variance given the effective volume considered and θ_{norm}^2 captures the overall amplitude of the covariance matrix \mathbf{S} . The strength of cosmic variance within our simulation volume shall satisfy $\alpha_{\text{cv}} = \sqrt{k^3 / \tilde{N}_k}$ at all scales k , where \tilde{N}_k is the effective number of modes at scale k , accounting for the window function. As in Leclercq *et al.* (2019), the hyperparameters k_{corr} and θ_{norm} are optimised to reproduce the shape of a fiducial wiggle vector $\boldsymbol{\theta}_{\text{fid}}$, using the effective posterior distribution obtained in Section II B 2 as the likelihood; that is,

$$-2 \log \mathcal{P}(k_{\text{corr}}, \theta_{\text{norm}} | \boldsymbol{\theta}) \equiv \log |2\pi \mathbf{\Gamma}| + \|\boldsymbol{\theta}_{\text{fid}} - \boldsymbol{\gamma}\|_{\mathbf{\Gamma}^{-1}}, \quad (\text{C5})$$

where $\boldsymbol{\gamma}$ and $\mathbf{\Gamma}$ inherit their dependence on k_{corr} and θ_{norm} through \mathbf{S} . We use Gaussian hyperpriors on $(k_{\text{corr}}, \theta_{\text{norm}})$, namely $k_{\text{corr}} \sim \mathcal{G}(0.020, 0.015^2)$ [$h \text{ Mpc}^{-1}$] and $\theta_{\text{norm}} \sim \mathcal{G}(0.2, 0.3^2)$. We estimated the maximum *a posteriori* using L-BFGS (Liu & Nocedal, 1989) and found $k_{\text{corr}} = 0.012458 h \text{ Mpc}^{-1}$ and $\theta_{\text{norm}} = 0.034743$, values that were used to obtain the prior on $\boldsymbol{\theta}$ corresponding to the shaded yellow area in Figure 14.

The posterior obtained with the wiggle-less prior is in green in Figure 14. It is consistent with the ground truth. Notably, it accurately retrieves the oscillations up to $k \simeq 0.2 h/\text{Mpc}$, even though the prior is completely agnostic to the BAOs, except through its hyperparameter optimisation.

D. IMPACT OF LINEAR GALAXY BIAS PARAMETERS

The linear galaxy bias parameters have a quadratic scale-independent impact on the galaxy overdensity power spectrum. We show qualitatively that this is expected to hold true for the SELFIE posterior, to some extent. Indeed, neglecting the term $\mathbf{\Gamma} \mathbf{S}^{-1} \boldsymbol{\Delta}$, which we measured to be smaller than 10^{-3} at all scales in our set-up, the SELFIE filter equation (20) for the mean of the posterior on the matter power spectrum can be rewritten:

$$\boldsymbol{\gamma} = \boldsymbol{\theta}_0 + \mathbf{\Gamma} (\nabla_{\boldsymbol{\theta}} \mathbf{f}_0)^\top \mathbf{C}_0^{-1} \boldsymbol{\Phi}_O - \mathbf{\Gamma} (\nabla_{\boldsymbol{\theta}} \mathbf{f}_0)^\top \mathbf{C}_0^{-1} \mathbf{f}_0. \quad (\text{D1})$$

If we consider for simplicity the case where the overall noise level is $\sigma = 0$, for a fixed phase, $P^{\mathcal{E}_i}(k_r)$ becomes a deterministic function of b_{g_i} given by

$$P^{\mathcal{E}_i}(k_r) \propto b_{g_i}^2 \sum_{|\mathbf{k}|=k_r} \left| \widehat{\mathbf{W}_i \boldsymbol{\delta}^{z_i}}(k) \right|^2,$$

where $\widehat{\mathbf{h}}$ denotes the discrete Fourier transform of \mathbf{h} . Hence, in the absence of noise, a constant relative error on all the three squared linear galaxy biases has a

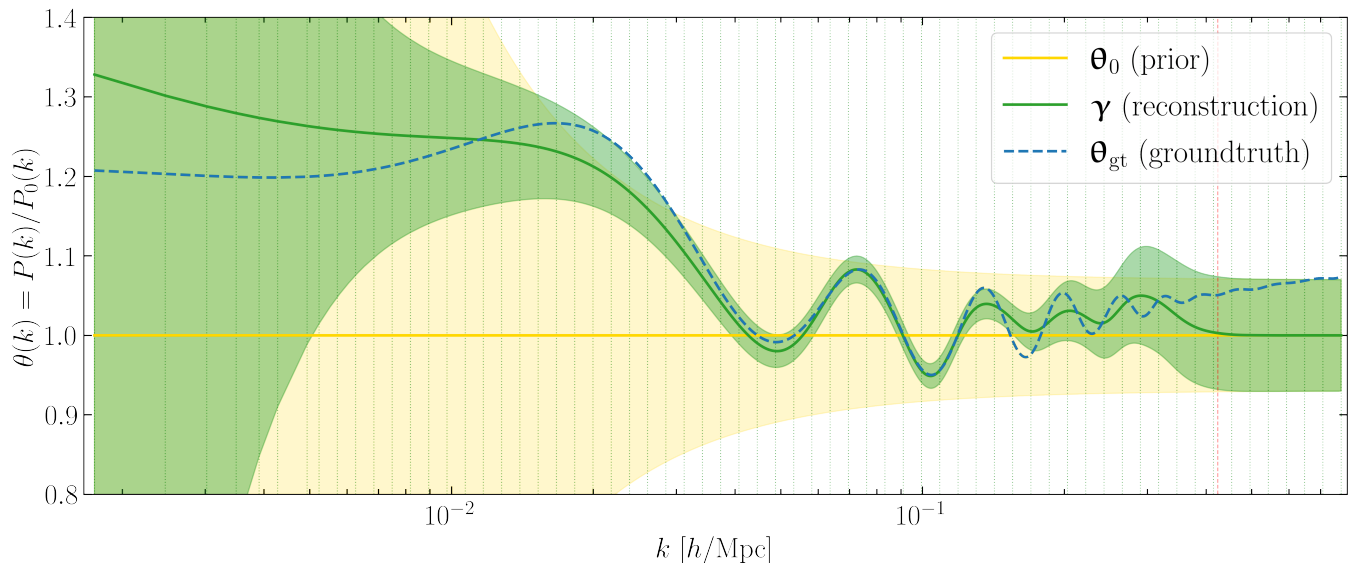


FIG. 14. Wiggle-less prior and corresponding SELFIE posterior on the initial matter power spectrum θ . The prior mean θ_0 , also used as expansion point, is indicated by the yellow line; its 2σ credible region corresponds to the yellow-shaded area. The posterior mean γ and 2σ credible region correspond to the green line and shaded area. The ground truth θ_{gt} is indicated by the solid blue line. The dashed red line denotes the Nyquist frequency. Even though the prior contains no information about the BAOs, the SELFIE posterior is consistently unbiased across all scales and accurately retrieves the oscillations up to $k \simeq 0.2 h/\text{Mpc}$.

scale-independent impact on any simulated summary Φ obtained with the hidden-box simulator. By linearity of the \mathbb{E} and ∂_θ operators, the relative impacts on \mathbf{f}_0 and $\nabla_\theta \mathbf{f}_0$ are scale-independent as well and quadratic in b_{g_i} . Similarly, from Equation (13), \mathbf{C}_0^{-1} scales as $b_{g_i}^{-4}$, so that, from Equation (21), Γ and therefore $\Gamma(\nabla_\theta \mathbf{f}_0)^\top \mathbf{C}_0^{-1} \mathbf{f}_0$ are left unaffected and only the $\Gamma(\nabla_\theta \mathbf{f}_0)^\top \mathbf{C}_0^{-1} \Phi_0$ term in Equation (D1) is impacted by misspecified galaxy biases. If the misspecified biases are such that the relative error $(b_i^{\text{mis}})^2/b_{g_i}^2 = \epsilon$ is independent of the population g_i , then every component of the vector $(\nabla_\theta \mathbf{f}_0)^\top \mathbf{C}_0^{-1} \Phi_0$ is affected by a factor ϵ , and the overall effect inherits its scale-dependence solely through the covariance matrix Γ . This is the behaviour observed on Figure 9a, where, for a misspecified bias, all the scales undergo about the same shift in number of standard deviations.

E. IMPLICIT LIKELIHOOD INFERENCE OF COSMOLOGICAL PARAMETERS

1. Numerical set-up

For the ILI of cosmological parameters, we used the variant of ABC-PMC from Simola *et al.* (2021) implemented in the ELFI package (github.com/elfi-dev/elfi, Lintusaari *et al.*, 2018), with minor technical modifications which do not affect the statistical method.

2. Population Monte Carlo hyperparameters

The Population Monte Carlo algorithm automatically selects a tolerance sequence based on the procedure described by Simola *et al.* (2021). It is not completely ϵ -free as one must choose a stopping rule and an initial acceptance threshold for the rejection sampler, the choice of the latter being crucial to prevent the algorithm from getting stuck in local overdense regions of the parameter space. In this study, we set the initial quantile used to determine the corresponding acceptance threshold for the rejection sampling stage to $q_0 = 0.2$.

ACKNOWLEDGMENTS

We thank Chloé Barjou-Delayre, Guilhem Lavaux ([ID](#)), Gary Mamon ([ID](#)), Nhat-Minh Nguyen ([ID](#)) and Fabian Schmidt ([ID](#)) for useful discussions and feedback to enhance this manuscript. The work has made use of the Infinity Cluster hosted by the Institut d’Astrophysique de Paris. We appreciate the efforts of Stéphane Rouberol for running the cluster smoothly. FL and TH acknowledge financial support from the Agence Nationale de la Recherche (ANR) through the grant INFOCW, under reference ANR-23-CE46-0006-01. FL and TH acknowledge financial support from the Simons Collaboration on “Learning the Universe”. This work was done within the Aquila Consortium (<https://www.aquila-consortium.org/>).

REFERENCES

- (Addison *et al.*, 2019) G. E. Addison, C. L. Bennett, D. Jeong, E. Komatsu, J. L. Weiland, *The Impact of Line Misidentification on Cosmological Constraints from Euclid and Other Spectroscopic Galaxy Surveys*, *Astrophys. J.* **879**, 15 (2019), arXiv:1811.10668 [astro-ph.CO].
- (Albrecht *et al.*, 2006) A. Albrecht, G. Bernstein, R. Cahn, W. L. Freedman, J. Hewitt, W. Hu, J. Huth, M. Kamionkowski, E. W. Kolb, L. Knox, *et al.*, *Report of the Dark Energy Task Force*, arXiv e-prints 10.48550/arXiv.astro-ph/0609591 (2006), arXiv:astro-ph/0609591.
- (Alsing & Wandelt, 2018) J. Alsing, B. Wandelt, *Generalized massive optimal data compression*, *Mon. Not. R. Astron. Soc.* **476**, L60 (2018), arXiv:1712.00012 [astro-ph.CO].
- (Alsing, Wandelt & Feeney, 2018) J. Alsing, B. Wandelt, S. Feeney, *Massive optimal data compression and density estimation for scalable, likelihood-free inference in cosmology*, *Mon. Not. R. Astron. Soc.* **477**, 2874 (2018), arXiv:1801.01497 [astro-ph.CO].
- (Alsing *et al.*, 2019) J. Alsing, T. Charnock, S. Feeney, B. Wandelt, *Fast likelihood-free cosmology with neural density estimators and active learning*, *Mon. Not. R. Astron. Soc.* **488**, 4440 (2019), arXiv:1903.00007 [astro-ph.CO].
- (Alsing *et al.*, 2016) J. Alsing, A. Heavens, A. H. Jaffe, A. Kiessling, B. Wandelt, T. Hoffmann, *Hierarchical cosmic shear power spectrum inference*, *Mon. Not. R. Astron. Soc.* **455**, 4452 (2016), arXiv:1505.07840 [astro-ph.CO].
- (Anderson *et al.*, 2014) L. Anderson, É. Aubourg, S. Bailey, F. Beutler, V. Bhardwaj, M. Blanton, A. S. Bolton, J. Brinkmann, J. R. Brownstein, A. Burden, *et al.*, *The clustering of galaxies in the SDSS-III Baryon Oscillation Spectroscopic Survey: baryon acoustic oscillations in the Data Releases 10 and 11 Galaxy samples*, *Mon. Not. R. Astron. Soc.* **441**, 24 (2014), arXiv:1312.4877 [astro-ph.CO].
- (Andrews *et al.*, 2023) A. Andrews, J. Jasche, G. Lavaux, F. Schmidt, *Bayesian field-level inference of primordial non-Gaussianity using next-generation galaxy surveys*, *Mon. Not. R. Astron. Soc.* **520**, 5746 (2023), arXiv:2203.08838 [astro-ph.CO].
- (Arnalte-Mur *et al.*, 2016) P. Arnalte-Mur, P. Vielva, V. J. Martínez, J. L. Sanz, E. Saar, S. Paredes, *Joint constraints on galaxy bias and σ_8 through the N -pdf of the galaxy number density*, *J. Cosmology Astropart. Phys.* **2016**, 005 (2016), arXiv:1506.07794 [astro-ph.CO].
- (Ayçoberry *et al.*, 2023) E. Ayçoberry, V. Ajani, A. Guinot, M. Kilbinger, V. Pettorino, S. Farrens, J.-L. Starck, R. Gavazzi, M. J. Hudson, *UNIONS: The impact of systematic errors on weak-lensing peak counts*, *Astron. & Astrophys.* **671**, A17 (2023), arXiv:2204.06280 [astro-ph.CO].
- (Balkenhol *et al.*, 2023) L. Balkenhol, D. Dutcher, A. Spurio Mancini, A. Doussot, K. Benabed, S. Galli, P. A. R. Ade, A. J. Anderson, B. Ansarinejad, M. Archipley, *et al.*, *Measurement of the CMB temperature power spectrum and constraints on cosmology from the SPT-3G 2018 TT , TE , and EE dataset*, *Phys. Rev. D* **108**, 023510 (2023), arXiv:2212.05642 [astro-ph.CO].
- (Bardeen *et al.*, 1986) J. M. Bardeen, J. R. Bond, N. Kaiser, A. S. Szalay, *The Statistics of Peaks of Gaussian Random Fields*, *Astrophys. J.* **304**, 15 (1986).
- (Barreira, 2020) A. Barreira, *On the impact of galaxy bias uncertainties on primordial non-Gaussianity constraints*, *J. Cosmology Astropart. Phys.* **2020**, 031 (2020), arXiv:2009.06622 [astro-ph.CO].
- (Barreira, Lazeyras & Schmidt, 2021) A. Barreira, T. Lazeyras, F. Schmidt, *Galaxy bias from forward models: linear and second-order bias of IllustrisTNG galaxies*, *J. Cosmology Astropart. Phys.* **2021**, 029 (2021), arXiv:2105.02876 [astro-ph.CO].
- (Barreira *et al.*, 2020) A. Barreira, G. Cabass, K. D. Lozanov, F. Schmidt, *Compensated isocurvature perturbations in the galaxy power spectrum*, *J. Cosmology Astropart. Phys.* **2020**, 049 (2020), arXiv:2002.12931 [astro-ph.CO].
- (Bartlett, Ho & Wandelt, 2024) D. J. Bartlett, M. Ho, B. D. Wandelt, *Bye-bye, Local-in-matter-density Bias: The Statistics of the Halo Field Are Poorly Determined by the Local Mass Density*, *Astrophys. J. Lett.* **977**, L44 (2024), arXiv:2405.00635 [astro-ph.CO].
- (Beaumont, Zhang & Balding, 2002) M. A. Beaumont, W. Zhang, D. J. Balding, *Approximate Bayesian Computation in Population Genetics*, *Genetics* **162**, 2025 (2002).
- (Beaumont *et al.*, 2009) M. A. Beaumont, J.-M. Cornuet, J.-M. Marin, C. P. Robert, *Adaptive approximate Bayesian computation*, *Biometrika* **96**, 983 (2009), <https://academic.oup.com/biomet/article-pdf/96/4/983/588237/asp052.pdf>.
- (Berti, Dawson & Dominguez, 2023) A. M. Berti, K. S. Dawson, W. Dominguez, *The Galaxy-Halo Connection of DESI Luminous Red Galaxies with Subhalo Abundance Matching*, *Astrophys. J.* **954**, 131 (2023), arXiv:2303.16096 [astro-ph.CO].
- (Beutler *et al.*, 2012) F. Beutler, C. Blake, M. Colless, D. H. Jones, L. Staveley-Smith, G. B. Poole, L. Campbell, Q. Parker, W. Saunders, F. Watson, *The 6dF Galaxy Survey: $z \approx 0$ measurements of the growth rate and σ_8* , *Mon. Not. R. Astron. Soc.* **423**, 3430 (2012), arXiv:1204.4725 [astro-ph.CO].
- (Beyond-2pt Collaboration, 2024) Beyond-2pt Collaboration, *A Parameter-Masked Mock Data Challenge for Beyond-Two-Point Galaxy Clustering Statistics*, arXiv e-prints, arXiv:2405.02252 (2024), arXiv:2405.02252 [astro-ph.CO].
- (Blas, Lesgourgues & Tram, 2011) D. Blas, J. Lesgourgues, T. Tram, *The Cosmic Linear Anisotropy Solving System (CLASS). Part II: Approximation schemes*, *J. Cosmology Astropart. Phys.* **2011**, 034 (2011), arXiv:1104.2933 [astro-ph.CO].
- (Blumenthal *et al.*, 1984) G. R. Blumenthal, S. M. Faber, J. R. Primack, M. J. Rees, *Formation of galaxies and large-scale structure with cold dark matter.*, *Nature* **311**, 517 (1984).
- (Bouchet *et al.*, 1995) F. R. Bouchet, S. Colombi, E. Hivon, R. Juszkiewicz, *Perturbative Lagrangian approach to gravitational instability.*, *Astron. & Astrophys.* **296**, 575 (1995), arXiv:astro-ph/9406013 [astro-ph].
- (Boulanger *et al.*, 1996) F. Boulanger, A. Abergel, J. P. Bernard, W. B. Burton, F. X. Desert, D. Hartmann, G. Lagache, J. L. Puget, *The dust/gas correlation at high Galactic latitude.*, *Astron. & Astrophys.* **312**, 256 (1996).
- (Bovy *et al.*, 2016) J. Bovy, H.-W. Rix, G. M. Green, E. F. Schlafly, D. P. Finkbeiner, *On Galactic Density Modeling in the Presence of Dust Extinction*, *Astrophys. J.* **818**, 130 (2016), arXiv:1509.06751 [astro-ph.GA].
- (Brehmer *et al.*, 2018) J. Brehmer, G. Louppe, J. Pavez, K. Cranmer, *Mining gold from implicit models to improve likelihood-free inference*, arXiv e-prints, arXiv:1805.12244 (2018), arXiv:1805.12244 [stat.ML].
- (Brout & Riess, 2023) D. Brout, A. Riess, *The Impact of Dust on Cepheid and Type Ia Supernova Distances*, arXiv e-prints, arXiv:2311.08253 (2023), arXiv:2311.08253 [astro-ph.CO].
- (Campagne *et al.*, 2023) J.-E. Campagne, F. Lanusse, J. Zuntz, A. Boucaud, S. Casas, M. Karamanis, D. Kirkby, D. Lanzieri, A. Peel, Y. Li, *JAX-COSMO: An End-to-End Differentiable and GPU Accelerated Cosmology Library*, *The Open Journal of Astrophysics* **6**, 15 (2023), arXiv:2302.05163 [astro-ph.CO].
- (Carreres *et al.*, 2023) B. Carreres, J. E. Bautista, F. Feinstein, D. Fouchez, B. Racine, M. Smith, M. Amenouche, M. Aubert, S. Dhawan, M. Ginolin, *et al.*, *Growth-rate measurement with type-Ia supernovae using ZTF survey simulations*, *Astron. & Astrophys.* **674**, A197 (2023), arXiv:2303.01198 [astro-ph.CO].
- (Charnock, Lavaux & Wandelt, 2018) T. Charnock, G. Lavaux, B. D. Wandelt, *Automatic physical inference with information maximizing neural networks*, *Phys. Rev. D* **97**, 083004 (2018), arXiv:1802.03537 [astro-ph.IM].
- (Colless *et al.*, 2001) M. Colless, G. Dalton, S. Maddox, W. Sutherland, P. Norberg, S. Cole, J. Bland-Hawthorn, T. Bridges,

- R. Cannon, C. Collins, *et al.*, *The 2df galaxy redshift survey: spectra and redshifts*, Monthly Notices of the Royal Astronomical Society **328**, 1039 (2001).
- (Corasaniti, 2006) P. S. Corasaniti, *The impact of cosmic dust on supernova cosmology*, Mon. Not. R. Astron. Soc. **372**, 191 (2006), arXiv:astro-ph/0603833 [astro-ph].
- (Cranmer, Brehmer & Louppe, 2020) K. Cranmer, J. Brehmer, G. Louppe, *The frontier of simulation-based inference*, Proceedings of the National Academy of Science **117**, 30055 (2020), arXiv:1911.01429 [stat.ML].
- (Davis *et al.*, 2011) T. M. Davis, L. Hui, J. A. Frieman, T. Haugbølle, R. Kessler, B. Sinclair, J. Sollerman, B. Bassett, J. Marriner, E. Mörtzell, *et al.*, *The Effect of Peculiar Velocities on Supernova Cosmology*, Astrophys. J. **741**, 67 (2011), arXiv:1012.2912 [astro-ph.CO].
- (DESI Collaboration, 2016) DESI Collaboration, *The DESI Experiment Part I: Science, Targeting, and Survey Design*, arXiv e-prints, arXiv:1611.00036 (2016), arXiv:1611.00036 [astro-ph.IM].
- (Desjacques, Jeong & Schmidt, 2018) V. Desjacques, D. Jeong, F. Schmidt, *Large-scale galaxy bias*, Phys. Rep. **733**, 1 (2018), arXiv:1611.09787 [astro-ph.CO].
- (Ding, Lavaux & Jasche, 2024) S. Ding, G. Lavaux, J. Jasche, *Pine-Tree: A generative, fast, and differentiable halo model for wide-field galaxy surveys*, Astron. & Astrophys. **690**, A236 (2024), arXiv:2407.01391 [astro-ph.CO].
- (Doerer *et al.*, 2024) L. Doerer, D. Jamieson, S. Stopyra, G. Lavaux, F. Leclercq, J. Jasche, *Bayesian inference of initial conditions from non-linear cosmic structures using field-level emulators*, Mon. Not. R. Astron. Soc. **535**, 1258 (2024), arXiv:2312.09271 [astro-ph.CO].
- (Duane *et al.*, 1987) S. Duane, A. D. Kennedy, B. J. Pendleton, D. Roweth, *Hybrid Monte Carlo*, Physics Letters B **195**, 216 (1987).
- (Eisenstein, 2015) D. Eisenstein, *The Baryon Oscillation Spectroscopic Survey (BOSS): Dark Energy from the World's Largest Redshift Survey*, in *APS April Meeting Abstracts*, APS Meeting Abstracts, Vol. 2015 (2015) p. Z2.001.
- (Eisenstein & Hu, 1998) D. J. Eisenstein, W. Hu, *Baryonic Features in the Matter Transfer Function*, Astrophys. J. **496**, 605 (1998), arXiv:astro-ph/9709112 [astro-ph].
- (Eisenstein *et al.*, 2001) D. J. Eisenstein, J. Annis, J. E. Gunn, A. S. Szalay, A. J. Connolly, R. C. Nichol, N. A. Bahcall, M. Bernardi, S. Burles, F. J. Castander, *et al.*, *Spectroscopic Target Selection for the Sloan Digital Sky Survey: The Luminous Red Galaxy Sample*, Astron. J. **122**, 2267 (2001), arXiv:astro-ph/0108153 [astro-ph].
- (Eisenstein *et al.*, 2005) D. J. Eisenstein, I. Zehavi, D. W. Hogg, R. Scoccimarro, M. R. Blanton, R. C. Nichol, R. Scranton, H.-J. Seo, M. Tegmark, Z. Zheng, *et al.*, *Detection of the Baryon Acoustic Peak in the Large-Scale Correlation Function of SDSS Luminous Red Galaxies*, Astrophys. J. **633**, 560 (2005), arXiv:astro-ph/0501171 [astro-ph].
- (Euclid Collaboration, 2024) Euclid Collaboration, *Euclid. I. Overview of the Euclid mission*, arXiv e-prints, arXiv:2405.13491 (2024), arXiv:2405.13491 [astro-ph.CO].
- (Euclid Collaboration, 2020) Euclid Collaboration, *Euclid preparation. VII. Forecast validation for Euclid cosmological probes*, Astron. & Astrophys. **642**, A191 (2020), arXiv:1910.09273 [astro-ph.CO].
- (Fazolo, Amendola & Velten, 2022) R. E. Fazolo, L. Amendola, H. Velten, *Skewness as a test of dark energy perturbations*, Phys. Rev. D **105**, 103521 (2022).
- (Frazier, Robert & Rousseau, 2017) D. T. Frazier, C. P. Robert, J. Rousseau, *Model Misspecification in ABC: Consequences and Diagnostics*, arXiv e-prints, arXiv:1708.01974 (2017), arXiv:1708.01974 [math.ST].
- (Galametz *et al.*, 2017) A. Galametz, R. Saglia, S. Paltani, N. Apostolakis, P. Dubath, *SED-dependent galactic extinction prescription for Euclid and future cosmological surveys*, Astron. & Astrophys. **598**, A20 (2017), arXiv:1609.08624 [astro-ph.CO].
- (Gavazzi & Jaffe, 1986) G. Gavazzi, W. Jaffe, *Radio Continuum Survey of the Coma/A1367 Supercluster. III. Radio Properties of Galaxies in Different Density Environments*, Astrophys. J. **310**, 53 (1986).
- (Gil-Marín *et al.*, 2015) H. Gil-Marín, J. Noreña, L. Verde, W. J. Percival, C. Wagner, M. Manera, D. P. Schneider, *The power spectrum and bispectrum of SDSS DR11 BOSS galaxies - I. Bias and gravity*, Mon. Not. R. Astron. Soc. **451**, 539 (2015), arXiv:1407.5668 [astro-ph.CO].
- (Glanville, Howlett & Davis, 2021) A. Glanville, C. Howlett, T. M. Davis, *The effect of systematic redshift biases in BAO cosmology*, Mon. Not. R. Astron. Soc. **503**, 3510 (2021), arXiv:2011.04210 [astro-ph.CO].
- (Goldstein *et al.*, 2023) S. Goldstein, M. Park, M. Raveri, B. Jain, L. Samushia, *Beyond dark energy Fisher forecasts: How the Dark Energy Spectroscopic Instrument will constrain LCDM and quintessence models*, Phys. Rev. D **107**, 063530 (2023), arXiv:2207.01612 [astro-ph.CO].
- (Hahn, List & Porqueres, 2024) O. Hahn, F. List, N. Porqueres, *DISCO-DJ I: a differentiable Einstein-Boltzmann solver for cosmology*, J. Cosmology Astropart. Phys. **2024**, 063 (2024), arXiv:2311.03291 [astro-ph.CO].
- (Hartlap, Simon & Schneider, 2007) J. Hartlap, P. Simon, P. Schneider, *Why your model parameter confidences might be too optimistic. Unbiased estimation of the inverse covariance matrix*, Astron. & Astrophys. **464**, 399 (2007), arXiv:astro-ph/0608064 [astro-ph].
- (Heavens, Jimenez & Lahav, 2000) A. F. Heavens, R. Jimenez, O. Lahav, *Massive lossless data compression and multiple parameter estimation from galaxy spectra*, Mon. Not. R. Astron. Soc. **317**, 965 (2000), arXiv:astro-ph/9911102 [astro-ph].
- (Ho *et al.*, 2024) M. Ho, D. J. Bartlett, N. Chartier, C. Cuesta-Lazaro, S. Ding, A. Lapel, P. Lemos, C. C. Lovell, T. L. Makinen, C. Modi, *et al.*, *LtU-ILL: An All-in-One Framework for Implicit Inference in Astrophysics and Cosmology*, The Open Journal of Astrophysics **7**, 54 (2024), arXiv:2402.05137 [astro-ph.IM].
- (Ho *et al.*, 2015) S. Ho, N. Agarwal, A. D. Myers, R. Lyons, A. Disbrow, H.-J. Seo, A. Ross, C. Hirata, N. Padmanabhan, R. O'Connell, *et al.*, *Sloan Digital Sky Survey III photometric quasar clustering: probing the initial conditions of the Universe*, J. Cosmology Astropart. Phys. **2015**, 040 (2015), arXiv:1311.2597 [astro-ph.CO].
- (Hockney & Eastwood, 1988) R. W. Hockney, J. W. Eastwood, *Computer simulation using particles* (Taylor & Francis Group, 1988).
- (Howlett *et al.*, 2015) C. Howlett, A. J. Ross, L. Samushia, W. J. Percival, M. Manera, *The clustering of the SDSS main galaxy sample - II. Mock galaxy catalogues and a measurement of the growth of structure from redshift space distortions at $z = 0.15$* , Mon. Not. R. Astron. Soc. **449**, 848 (2015), arXiv:1409.3238 [astro-ph.CO].
- (Huterer, Cunha & Fang, 2013) D. Huterer, C. E. Cunha, W. Fang, *Calibration errors unleashed: effects on cosmological parameters and requirements for large-scale structure surveys*, Mon. Not. R. Astron. Soc. **432**, 2945 (2013), arXiv:1211.1015 [astro-ph.CO].
- (Ishida *et al.*, 2015) E. E. Ishida, S. D. Vitenti, M. Penna-Lima, J. Cisewski, R. S. de Souza, A. M. Trindade, E. Cameron, V. C. Busti, C. collaboration, others, *Cosmoabc: likelihood-free inference via population Monte Carlo approximate Bayesian computation*, Astronomy and Computing **13**, 1 (2015).
- (Ivezić *et al.*, 2019) Ž. Ivezić, S. M. Kahn, J. A. Tyson, B. Abel, E. Acosta, R. Allsman, D. Alonso, Y. AlSayyad, S. F. Anderson, J. Andrew, *et al.*, *LSST: from science drivers to reference design and anticipated data products*, The Astrophysical Journal **873**, 111 (2019).
- (Jasche & Lavaux, 2019) J. Jasche, G. Lavaux, *Physical Bayesian modelling of the non-linear matter distribution: New insights into the nearby universe*, Astron. & Astrophys. **625**, A64 (2019), arXiv:1806.11117 [astro-ph.CO].

- (Jasche & Wandelt, 2013) J. Jasche, B. D. Wandelt, *Bayesian physical reconstruction of initial conditions from large-scale structure surveys*, *Mon. Not. R. Astron. Soc.* **432**, 894 (2013), arXiv:1203.3639 [astro-ph.CO].
- (Jasche & Lavaux, 2017) J. Jasche, G. Lavaux, *Bayesian power spectrum inference with foreground and target contamination treatment*, *Astron. & Astrophys.* **606**, A37 (2017), arXiv:1706.08971 [astro-ph.CO].
- (Jasche et al., 2010) J. Jasche, F. S. Kitaura, B. D. Wandelt, T. A. EnBlin, *Bayesian power-spectrum inference for large-scale structure data*, *Mon. Not. R. Astron. Soc.* **406**, 60 (2010), arXiv:0911.2493 [astro-ph.CO].
- (Kaiser, 1984) N. Kaiser, *On the spatial correlations of Abell clusters.*, *Astrophys. J. Lett.* **284**, L9 (1984).
- (Karchev et al., 2024) K. Karchev, M. Grayling, B. M. Boyd, R. Trotta, K. S. Mandel, C. Weniger, *SIDE-real: Supernova Ia Dust Extinction with truncated marginal neural ratio estimation applied to real data*, *Mon. Not. R. Astron. Soc.* **530**, 3881 (2024), arXiv:2403.07871 [astro-ph.CO].
- (Kim et al., 2004) A. G. Kim, E. V. Linder, R. Miquel, N. Mostek, *Effects of systematic uncertainties on the supernova determination of cosmological parameters*, *Mon. Not. R. Astron. Soc.* **347**, 909 (2004), arXiv:astro-ph/0304509 [astro-ph].
- (Kitching, Taylor & Heavens, 2008) T. D. Kitching, A. N. Taylor, A. F. Heavens, *Systematic effects on dark energy from 3D weak shear*, *Mon. Not. R. Astron. Soc.* **389**, 173 (2008), arXiv:0801.3270 [astro-ph].
- (Kitching et al., 2016) T. D. Kitching, L. Verde, A. F. Heavens, R. Jimenez, *Discrepancies between CFHTLenS cosmic shear and Planck: new physics or systematic effects?*, *Mon. Not. R. Astron. Soc.* **459**, 971 (2016), arXiv:1602.02960 [astro-ph.CO].
- (Kostić et al., 2023) A. Kostić, N.-M. Nguyen, F. Schmidt, M. Reinecke, *Consistency tests of field level inference with the EFT likelihood*, *J. Cosmology Astropart. Phys.* **2023**, 063 (2023), arXiv:2212.07875 [astro-ph.CO].
- (Kullback & Leibler, 1951) S. Kullback, R. A. Leibler, *On information and sufficiency*, *The annals of mathematical statistics* **22**, 79 (1951).
- (Lanzieri et al., 2024) D. Lanzieri, J. Zeghal, T. L. Makinen, A. Boucaud, J.-L. Starck, F. Lanusse, *Optimal Neural Summarisation for Full-Field Weak Lensing Cosmological Implicit Inference*, arXiv e-prints , arXiv:2407.10877 (2024), arXiv:2407.10877 [astro-ph.CO].
- (Laureijs et al., 2011) R. Laureijs, J. Amiaux, S. Arduini, J. L. Augères, J. Brinchmann, R. Cole, M. Cropper, C. Dabin, L. Duvel, A. Ealet, et al., *Euclid Definition Study Report*, arXiv e-prints , arXiv:1110.3193 (2011), arXiv:1110.3193 [astro-ph.CO].
- (Leclercq, 2018) F. Leclercq, *Bayesian optimization for likelihood-free cosmological inference*, *Phys. Rev. D* **98**, 063511 (2018), arXiv:1805.07152 [astro-ph.CO].
- (Leclercq, 2022) F. Leclercq, *Simulation-Based Inference of Bayesian Hierarchical Models While Checking for Model Misspecification*, in *MaxEnt 2022* (MDPI, 2022).
- (Leclercq, Jasche & Wandelt, 2015) F. Leclercq, J. Jasche, B. Wandelt, *Bayesian analysis of the dynamic cosmic web in the SDSS galaxy survey*, *J. Cosmology Astropart. Phys.* **2015**, 015 (2015), arXiv:1502.02690 [astro-ph.CO].
- (Leclercq et al., 2019) F. Leclercq, W. Enzi, J. Jasche, A. Heavens, *Primordial power spectrum and cosmology from black-box galaxy surveys*, *Mon. Not. R. Astron. Soc.* **490**, 4237 (2019), arXiv:1902.10149 [astro-ph.CO].
- (Leistedt & Peiris, 2014) B. Leistedt, H. V. Peiris, *Exploiting the full potential of photometric quasar surveys: optimal power spectra through blind mitigation of systematics*, *Mon. Not. R. Astron. Soc.* **444**, 2 (2014), arXiv:1404.6530 [astro-ph.CO].
- (Lewis & Challinor, 2011) A. Lewis, A. Challinor, *CAMB: Code for Anisotropies in the Microwave Background*, *Astrophysics Source Code Library* , ascl:1102.026 (2011).
- (Lintusaari et al., 2017) J. Lintusaari, M. U. Gutmann, R. Dutta, S. Kaski, J. Corander, *Fundamentals and recent developments in approximate Bayesian computation*, *Systematic biology* **66**, e66 (2017).
- (Lintusaari et al., 2018) J. Lintusaari, H. Vuollekoski, A. Kangasrääsiö, K. Skytén, M. Järvenpää, P. Marttinen, M. U. Gutmann, A. Vehtari, J. Corander, S. Kaski, *ELFI: Engine for Likelihood-Free Inference*, *Journal of Machine Learning Research* **19**, 1 (2018).
- (Liu & Nocedal, 1989) D. C. Liu, J. Nocedal, *On the limited memory BFGS method for large scale optimization*, *Mathematical programming* **45**, 503 (1989).
- (Loureiro et al., 2023) A. Loureiro, L. Whiteway, E. Sellentin, J. Silva Lafaurie, A. H. Jaffe, A. F. Heavens, *Almanac: Weak Lensing power spectra and map inference on the masked sphere*, *The Open Journal of Astrophysics* **6**, 6 (2023), arXiv:2210.13260 [astro-ph.CO].
- (LSST Dark Energy Science Collaboration, 2012) LSST Dark Energy Science Collaboration, *Large synoptic survey telescope: dark energy science collaboration*, arXiv preprint arXiv:1211.0310 (2012).
- (Makinen et al., 2021) T. L. Makinen, T. Charnock, J. Alsing, B. D. Wandelt, *Lossless, scalable implicit likelihood inference for cosmological fields*, *J. Cosmology Astropart. Phys.* **2021**, 049 (2021), arXiv:2107.07405 [astro-ph.CO].
- (Makinen et al., 2024) T. L. Makinen, A. Heavens, N. Porqueres, T. Charnock, A. Lapel, B. D. Wandelt, *Hybrid summary statistics: neural weak lensing inference beyond the power spectrum*, arXiv e-prints , arXiv:2407.18909 (2024), arXiv:2407.18909 [astro-ph.CO].
- (Massara et al., 2021) E. Massara, S. Ho, C. M. Hirata, J. DeRose, R. H. Wechsler, X. Fang, *Line confusion in spectroscopic surveys and its possible effects: shifts in Baryon Acoustic Oscillations position*, *Mon. Not. R. Astron. Soc.* **508**, 4193 (2021), arXiv:2010.00047 [astro-ph.CO].
- (Meiksin, White & Peacock, 1999) A. Meiksin, M. White, J. A. Peacock, *Baryonic signatures in large-scale structure*, *Mon. Not. R. Astron. Soc.* **304**, 851 (1999), arXiv:astro-ph/9812214 [astro-ph].
- (Ménard et al., 2008) B. Ménard, D. Nestor, D. Turnshek, A. Quider, G. Richards, D. Chelouche, S. Rao, *Lensing, reddening and extinction effects of Mg ii absorbers from $z=0.4$ to 2*, *Monthly Notices of the Royal Astronomical Society* **385**, 1053 (2008).
- (Metropolis et al., 1953) N. Metropolis, A. W. Rosenbluth, M. N. Rosenbluth, A. H. Teller, E. Teller, *Equation of state calculations by fast computing machines*, *The journal of chemical physics* **21**, 1087 (1953).
- (Mishra-Sharma, Alonso & Dunkley, 2018) S. Mishra-Sharma, D. Alonso, J. Dunkley, *Neutrino masses and beyond- Λ CDM cosmology with LSST and future CMB experiments*, *Phys. Rev. D* **97**, 123544 (2018), arXiv:1803.07561 [astro-ph.CO].
- (Modi, Lanusse & Seljak, 2021) C. Modi, F. Lanusse, U. Seljak, *FlowPM: Distributed TensorFlow implementation of the FastPM cosmological N-body solver*, *Astronomy and Computing* **37**, 100505 (2021), arXiv:2010.11847 [astro-ph.CO].
- (Mootoovaloo et al., 2022) A. Mootoovaloo, A. H. Jaffe, A. F. Heavens, F. Leclercq, *Kernel-based emulator for the 3D matter power spectrum from CLASS*, *Astronomy and Computing* **38**, 100508 (2022), arXiv:2105.02256 [astro-ph.CO].
- (More, Bovy & Hogg, 2009) S. More, J. Bovy, D. W. Hogg, *Cosmic Transparency: A Test with the Baryon Acoustic Feature and Type Ia Supernovae*, *Astrophys. J.* **696**, 1727 (2009), arXiv:0810.5553 [astro-ph].
- (Moutarde et al., 1991) F. Moutarde, J. M. Alimi, F. R. Bouchet, R. Pellat, A. Ramani, *Precollapse Scale Invariance in Gravitational Instability*, *Astrophys. J.* **382**, 377 (1991).
- (Neumann, 1951) V. Neumann, *Various techniques used in connection with random digits*, *Notes by GE Forsythe* , 36 (1951).
- (Nguyen et al., 2021) N.-M. Nguyen, F. Schmidt, G. Lavaux, J. Jasche, *Impacts of the physical data model on the forward*

- inference of initial conditions from biased tracers*, *J. Cosmology Astropart. Phys.* **2021**, 058 (2021), arXiv:2011.06587 [astro-ph.CO].
- (Nguyen *et al.*, 2024) N.-M. Nguyen, F. Schmidt, B. Tucci, M. Reinecke, A. Kostić, *How Much Information Can Be Extracted from Galaxy Clustering at the Field Level?*, *Phys. Rev. Lett.* **133**, 221006 (2024), arXiv:2403.03220 [astro-ph.CO].
- (Parzen, 1962) E. Parzen, *On estimation of a probability density function and mode*, *The annals of mathematical statistics* **33**, 1065 (1962).
- (Peebles, 1980) P. J. E. Peebles, *The large-scale structure of the universe* (Princeton University Press, 1980).
- (Philcox & Ivanov, 2022) O. H. E. Philcox, M. M. Ivanov, *BOSS DR12 full-shape cosmology: Λ CDM constraints from the large-scale galaxy power spectrum and bispectrum monopole*, *Phys. Rev. D* **105**, 043517 (2022), arXiv:2112.04515 [astro-ph.CO].
- (Planck Collaboration, 2020) Planck Collaboration, *Planck 2018 results. VI. Cosmological parameters*, *Astron. & Astrophys.* **641**, A6 (2020), arXiv:1807.06209 [astro-ph.CO].
- (Porqueres *et al.*, 2022) N. Porqueres, A. Heavens, D. Mortlock, G. Lavaux, *Lifting weak lensing degeneracies with a field-based likelihood*, *Mon. Not. R. Astron. Soc.* **509**, 3194 (2022), arXiv:2108.04825 [astro-ph.CO].
- (Porqueres *et al.*, 2019) N. Porqueres, D. Kodi Ramanah, J. Jasche, G. Lavaux, *Explicit Bayesian treatment of unknown foreground contaminations in galaxy surveys*, *Astron. & Astrophys.* **624**, A115 (2019), arXiv:1812.05113 [astro-ph.CO].
- (Prideaux-Ghee *et al.*, 2023) J. Prideaux-Ghee, F. Leclercq, G. Lavaux, A. Heavens, J. Jasche, *Field-based physical inference from peculiar velocity tracers*, *Mon. Not. R. Astron. Soc.* **518**, 4191 (2023), arXiv:2204.00023 [astro-ph.CO].
- (Pullen *et al.*, 2016) A. R. Pullen, C. M. Hirata, O. Doré, A. Raccañelli, *Interloper bias in future large-scale structure surveys*, *Pub. Astron. Soc. Japan* **68**, 12 (2016), arXiv:1507.05092 [astro-ph.CO].
- (Ramanah *et al.*, 2019) D. K. Ramanah, G. Lavaux, J. Jasche, B. D. Wandelt, *Cosmological inference from Bayesian forward modelling of deep galaxy redshift surveys*, *Astron. & Astrophys.* **621**, A69 (2019), arXiv:1808.07496 [astro-ph.CO].
- (Régald-Saint Blancard *et al.*, 2024) B. Régald-Saint Blancard, C. Hahn, S. Ho, J. Hou, P. Lemos, E. Massara, C. Modi, A. M. Dizgah, L. Parker, Y. Yao, *et al.*, *Galaxy clustering analysis with SimBIG and the wavelet scattering transform*, *Physical Review D* **109**, 083535 (2024).
- (Repp & Szapudi, 2020) A. Repp, I. Szapudi, *Galaxy bias and σ_8 from counts in cells from the SDSS main sample*, *Mon. Not. R. Astron. Soc.* **498**, L125 (2020), arXiv:2006.01146 [astro-ph.CO].
- (Rosenblatt, 1956) M. Rosenblatt, *Remarks on Some Nonparametric Estimates of a Density Function*, *The Annals of Mathematical Statistics* **27**, 832 (1956).
- (Ross *et al.*, 2013) A. J. Ross, W. J. Percival, A. Carnero, G.-b. Zhao, M. Manera, A. Raccañelli, E. Aubourg, D. Bizyaev, H. Brewington, J. Brinkmann, *et al.*, *The clustering of galaxies in the SDSS-III DR9 Baryon Oscillation Spectroscopic Survey: constraints on primordial non-Gaussianity*, *Mon. Not. R. Astron. Soc.* **428**, 1116 (2013), arXiv:1208.1491 [astro-ph.CO].
- (Said *et al.*, 2020) K. Said, M. Colless, C. Magoulas, J. R. Lucey, M. J. Hudson, *Joint analysis of 6dFGS and SDSS peculiar velocities for the growth rate of cosmic structure and tests of gravity*, *Mon. Not. R. Astron. Soc.* **497**, 1275 (2020), arXiv:2007.04993 [astro-ph.CO].
- (Salvati, Douspis & Aghanim, 2020) L. Salvati, M. Douspis, N. Aghanim, *Impact of systematics on cosmological parameters from future galaxy cluster surveys*, *Astron. & Astrophys.* **643**, A20 (2020), arXiv:2005.10204 [astro-ph.CO].
- (Sellentin *et al.*, 2023) E. Sellentin, A. Loureiro, L. Whiteway, J. S. Lafaurie, S. T. Balan, M. Olamaie, A. H. Jaffe, A. F. Heavens, *Almanac: MCMC-based signal extraction of power spectra and maps on the sphere*, *The Open Journal of Astrophysics* **6**, 31 (2023), arXiv:2305.16134 [astro-ph.CO].
- (Simola *et al.*, 2021) U. Simola, J. Cisewski-Kehe, M. U. Gutmann, J. Corander, *Adaptive Approximate Bayesian Computation Tolerance Selection*, *Bayesian Analysis* **16**, 397 (2021).
- (Spurio Mancini *et al.*, 2022) A. Spurio Mancini, D. Piras, J. Alsing, B. Joachimi, M. P. Hobson, *COSMOPOWER: emulating cosmological power spectra for accelerated Bayesian inference from next-generation surveys*, *Mon. Not. R. Astron. Soc.* **511**, 1771 (2022), arXiv:2106.03846 [astro-ph.CO].
- (Sunnåker *et al.*, 2013) M. Sunnåker, A. G. Busetto, E. Numminen, J. Corander, M. Foll, C. Dessimoz, *Approximate Bayesian Computation*, *PLoS Computational Biology* **9**, e1002803 (2013).
- (Tassev, Zaldarriaga & Eisenstein, 2013) S. Tassev, M. Zaldarriaga, D. J. Eisenstein, *Solving large scale structure in ten easy steps with COLA*, *J. Cosmology Astropart. Phys.* **2013**, 036 (2013), arXiv:1301.0322 [astro-ph.CO].
- (Taylor *et al.*, 2019) P. L. Taylor, T. D. Kitching, J. Alsing, B. D. Wandelt, S. M. Feeney, J. D. McEwen, *Cosmic shear: Inference from forward models*, *Phys. Rev. D* **100**, 023519 (2019), arXiv:1904.05364 [astro-ph.CO].
- (Tegmark *et al.*, 2004) M. Tegmark, M. A. Strauss, M. R. Blanton, K. Abazajian, S. Dodelson, H. Sandvik, X. Wang, D. H. Weinberg, I. Zehavi, N. A. Bahcall, *et al.*, *Cosmological parameters from SDSS and WMAP*, *Phys. Rev. D* **69**, 103501 (2004), arXiv:astro-ph/0310723 [astro-ph].
- (Thomas *et al.*, 2020) O. Thomas, R. Sá-Leão, H. de Lencastre, S. Kaski, J. Corander, H. Pesonen, *Misspecification-robust likelihood-free inference in high dimensions*, arXiv preprint arXiv:2002.09377 (2020).
- (Tucci & Schmidt, 2024) B. Tucci, F. Schmidt, *EFTofLSS meets simulation-based inference: σ_8 from biased tracers*, *J. Cosmology Astropart. Phys.* **2024**, 063 (2024), arXiv:2310.03741 [astro-ph.CO].
- (Wandelt, Larson & Lakshminarayanan, 2004) B. D. Wandelt, D. L. Larson, A. Lakshminarayanan, *Global, exact cosmic microwave background data analysis using Gibbs sampling*, *Phys. Rev. D* **70**, 083511 (2004), arXiv:astro-ph/0310080 [astro-ph].
- (Wang *et al.*, 2014) H. Wang, H. J. Mo, X. Yang, Y. P. Jing, W. P. Lin, *ELUCID—Exploring the Local Universe with the Reconstructed Initial Density Field. I. Hamiltonian Markov Chain Monte Carlo Method with Particle Mesh Dynamics*, *Astrophys. J.* **794**, 94 (2014), arXiv:1407.3451 [astro-ph.CO].
- (Wang *et al.*, 2016) H. Wang, H. J. Mo, X. Yang, Y. Zhang, J. Shi, Y. P. Jing, C. Liu, S. Li, X. Kang, Y. Gao, *ELUCID - Exploring the Local Universe with ReConstructed Initial Density Field III: Constrained Simulation in the SDSS Volume*, *Astrophys. J.* **831**, 164 (2016), arXiv:1608.01763 [astro-ph.CO].
- (Weyant, Schafer & Wood-Vasey, 2013) A. Weyant, C. Schafer, W. M. Wood-Vasey, *Likelihood-free Cosmological Inference with Type Ia Supernovae: Approximate Bayesian Computation for a Complete Treatment of Uncertainty*, *Astrophys. J.* **764**, 116 (2013), arXiv:1206.2563 [astro-ph.CO].
- (Zeghal *et al.*, 2024) J. Zeghal, D. Lanzieri, F. Lanusse, A. Boucaud, G. Louppe, E. Aubourg, A. E. Bayer, *The LSST Dark Energy Science Collaboration, Simulation-Based Inference Benchmark for LSST Weak Lensing Cosmology*, arXiv e-prints, arXiv:2409.17975 (2024), arXiv:2409.17975 [astro-ph.CO].
- (Zhou *et al.*, 2024) A. J. Zhou, X. Li, S. Dodelson, R. Mandelbaum, *Accurate field-level weak lensing inference for precision cosmology*, *Phys. Rev. D* **110**, 023539 (2024), arXiv:2312.08934 [astro-ph.CO].
- (Zhou *et al.*, 2023) R. Zhou, B. Dey, J. A. Newman, D. J. Eisenstein, K. Dawson, S. Bailey, A. Berti, J. Guy, T.-W. Lan, H. Zou, *et al.*, *Target Selection and Validation of DESI Luminous Red Galaxies*, *Astron. J.* **165**, 58 (2023), arXiv:2208.08515 [astro-ph.CO].